

Louisiana Tech University

Louisiana Tech Digital Commons

Doctoral Dissertations

Graduate School

Summer 8-16-2018

Smoothed Particle Hydrodynamics for Computational Fluid Dynamics

Wennan Ma

Louisiana Tech University

Follow this and additional works at: <https://digitalcommons.latech.edu/dissertations>

Recommended Citation

Ma, Wennan, "" (2018). *Dissertation*. 24.

<https://digitalcommons.latech.edu/dissertations/24>

This Dissertation is brought to you for free and open access by the Graduate School at Louisiana Tech Digital Commons. It has been accepted for inclusion in Doctoral Dissertations by an authorized administrator of Louisiana Tech Digital Commons. For more information, please contact digitalcommons@latech.edu.

Summer 8-16-2018

Smoothed Particle Hydrodynamics for Computational Fluid Dynamics

Wennan Ma

**SMOOTHED PARTICLE HYDRODYNAMICS FOR
COMPUTATIONAL FLUID DYNAMICS**

by

Wennan Ma, B. S., M. S.

A Thesis Presented in Partial Fulfillment
of the Requirements of the Degree
Doctor of Philosophy

May 2018

COLLEGE OF ENGINEERING AND SCIENCE
LOUISIANA TECH UNIVERSITY

LOUISIANA TECH UNIVERSITY

THE GRADUATE SCHOOL

May 7, 2018

Date

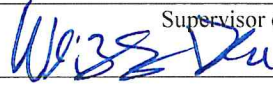
We hereby recommend that the dissertation prepared under our supervision
by Wennan Ma

entitled SMOOTHED PARTICLE HYDRODYNAMICS FOR
COMPUTATIONAL FLUID DYNAMICS

be accepted in partial fulfillment of the requirements for the Degree of
Doctor of Philosophy in Computational Analysis and Modeling



Supervisor of Dissertation Research



Head of Department

Computational Analysis and Modeling

Department

Recommendation concurred in:



Hou Songji

Advisory Committee

Weiguo Du

Approved:



Director of Graduate Studies

Approved:



Dean of the Graduate School



Dean of the College

ABSTRACT

Smoothed particle hydrodynamics (SPH) is a simple and effective numerical method that can be used to solve a variety of challenging problems in computational mechanics. It is a Lagrangian mesh-free method ideal for solving deformation problems. In the SPH method, the state of a system is represented by a set of particles, which possesses individual material properties and interact with each other within a specific range defined as a support domain by a weight function or smoothing function. SPH features flexibility in handling complex flow fields and in including physical effects.

In theory, the basic concept of the SPH method is introduced in this paper. Some detailed numerical aspects are discussed including the kernel approximation in continuous form and particle approximation in discrete form, the properties for the smoothing functions and some of the most frequently used ones in the SPH literature, the concept of support and interface domain, SPH formulations for Navier-Stokes equation, time integration, boundary treatment, particle interaction, artificial viscosity, laminar viscosity, shifting algorithm, and so on.

In applications, this paper presents an improved SPH method for modeling the diffusion process of a microneedle and using smoothed particle hydrodynamics (SPH) method to simulate the 25% cross-section stenosis blood vessel model and the 75% cross-section stenosis blood vessel model. The obtained numerical results are in close agreement with available theoretical and experimental results in the literature.

As an emerging transdermal drug delivery device, microneedles demonstrate some superior potential and advantages over traditional metallic needles-on-syringes in skin injection and vaccine [1]. However, very few research papers are available. This project uses a high order continuous method, the spectral element method (SEM), and a low order discrete method, the Smoothed Particle Hydrodynamics (SPH), to investigate this new drug delivery system. The incompressible Navier-Stokes equations were solved with SEM under appropriate initial and slip boundary conditions for the transport of medicine inside microneedles of rectangular and circular cross-sections. In addition, Darcy-Brinkman equations and a concentration equation were solved with SEM under appropriate initial and boundary conditions for the infiltration of medicine solution through porous media of the dermis tissue once a microneedle enters the skin. Meanwhile, the Lagrangian form of the Navier-Stokes equations were solved with the weighted interpolation approach via numerical integrations without inverting any matrices. Results from the mesh-based SEM and the mesh-free SPH simulations revealed technical details about the processes of delivery of medicine particles through microneedles and diffusion in the skin tissue, and the medicine concentration changes with space and time. The overall effect of medicine delivery under initial concentration and conditions were simulated and the effect of drug delivery were assessed.

The formation of thrombus is a complicated process. The existing literature rarely has a model for high-fidelity simulation of the effects and hazards of blood clots on blood flow. In this model, high-fidelity simulations are performed for complex human internal environments. The result of this simulation indicates high pressure area in blood vessel wall which matches the real condition of the vessel experiment.

Keywords: Smoothed particle hydrodynamics (SPH), micro-scale, micro-needle, thrombosis.

APPROVAL FOR SCHOLARLY DISSEMINATION

The author grants to the Prescott Memorial Library of Louisiana Tech University the right to reproduce, by appropriate methods, upon request, any or all portions of this Thesis. It is understood that “proper request” consists of the agreement, on the part of the requesting party, that said reproduction is for his personal use and that subsequent reproduction will not occur without written approval of the author of this Thesis. Further, any portions of the Thesis used in books, papers, and other works must be appropriately referenced to this Thesis.

Finally, the author of this Thesis reserves the right to publish freely, in the literature, at any time, any or all portions of this Thesis.

Author _____

Date _____

DEDICATION

This is dedicated to my parents, Yunjia Ma, Yanjing Xu, who love me, believe in me, inspire me, and have supported me every step of the way. Without their support and encouragement, I could never have walked this far.

TABLE OF CONTENTS

ABSTRACT.....	iii
APPROVAL FOR SCHOLARLY DISSEMINATION	vi
DEDICATION	vii
LIST OF FIGURES	xii
LIST OF TABLES	xiv
NOMENCLATURE	xv
ACKNOWLEDGMENTS	xvii
CHAPTER 1 INTRODUCTION	1
1.1 Motivation and Background	1
1.2 Background and applications of SPH method	3
1.3 Outline of Dissertation.....	6
CHAPTER 2 Literature REVIEW	9
2.1 The basic idea of the SPH method.....	9
2.2 Kernel approximation and particles approximation of SPH.....	10
2.2.1 Kernel approximation	10
2.2.2 Kernel approximation of derivatives	11
2.2.3 Particles approximation	12
2.3 Kernel function	14
2.3.1 Characteristics of kernel function	14
2.3.2 Kernel functions in the literature	16
2.3.2.1 The bell-shaped function.....	16

2.3.2.2	Gaussian kernel function.....	17
2.3.2.3	Cubic spline and B-spline kernel function.....	18
2.3.2.4	The fourth and fifth spline kernel functions	19
2.3.3	Approximate accuracy of SPH method.....	21
2.4	Consistency of SPH method	22
2.4.1	Consistency in kernel approximation.....	22
2.4.2	Consistency in particles approximation	23
2.5	SPH formulations for Navier-Stokes(N-S) equations.....	25
2.5.1	Particles approximation of density.....	25
2.5.2	Approximation of momentum equation.....	27
2.5.3	Approximation of energy equation	28
CHAPTER 3 CONTINUOUS AND DISCRETE SIMULATIONS OF MICRO-NEEDLES FOR EPIDERMAL DRUG DELIVERY		30
3.1	Introduction.....	31
3.2	Methodology.....	33
3.2.1	Discrete Modeling.....	33
3.2.1.1	Particles Interaction	35
3.2.1.2	Velocity Evaluation	35
3.3	Viscosity term.....	35
3.3.1	Artificial viscosity.....	36
3.3.2	Laminar viscosity.....	36
3.3.3	General viscosity.....	37
3.4	Artificial compressibility	38
3.5	Results and Discussion	39
3.5.1	Results for the SEM.....	39
3.5.1.1	Solution for Simulation of Micro-Needle	39

3.5.1.2	Solution for Simulation of Human Skin	44
3.5.1.2.1	Single Needle	44
3.5.1.2.2	Multiple Needles	47
3.5.2	SPH simulation results	50
3.6	3D microneedle simulation by SPH.....	54
3.7	Conclusion	58
CHAPTER 4 Constructing a thrombus model with SPH		60
4.1	Introduction.....	61
4.2	Time step.....	63
4.2.1	Verlet scheme.....	64
4.2.2	Symplectic scheme.....	64
4.3	Nearest neighbor particle search.....	66
4.3.1	All-pair search algorithm	66
4.3.2	Linked-list search algorithm	66
4.3.3	Tree search algorithm	69
4.4	Shifting algorithm	69
4.5	Boundary condition.....	71
4.5.1	The repulsive boundary conditions.....	72
4.5.2	Dynamic Boundary Condition	74
4.5.3	Periodic boundary	75
4.6	Result and discussion.....	76
4.6.1	Parameters and details about simulation.....	76
4.6.2	Velocity of blood flow in two models	78
4.6.3	Compare results with other simulation and experimental data.....	80
4.7	Conclusion	83

CHAPTER 5	85
5.1 Summary	85
5.2 Future work	86
Bibliography	88

LIST OF FIGURES

Figure 2-1: particles approximation in the support domain [4].	13
Figure 2-2: bellloid kernel function and its first derivative curve [15].	17
Figure 2-3: Gaussian kernel function and its first derivative curve [15].	18
Figure 2-4: plot of B-spline kernel function and its 1st order derivative curve [15].	19
Figure 2-5: the fourth spline kernel function and its 1st order derivative curve [15].	20
Figure 2-6: plot of fifth kernel function and its 1st order derivative curve [15].	21
Figure 3-1: the models of needles with circular and rectangular cross sections [85].	40
Figure 3-2: the pressure on xz-cross section [85].	41
Figure 3-3: the contours of velocity on z-direction at the inlet (up) and outlet (down) [85].	42
Figure 3-4: the contours of pressure at the inlet (up) and outlet (down) [85].	43
Figure 3-5: the initial contours of concentration with a different ratio of a needle's input area to the area of x-y cross section of model [85].	45
Figure 3-6: contour maps for single-needle model at t = 60 sections with different ratios of needle input area to the area of the x-y cross section [85].	46
Figure 3-7: the initial models of human skin with 4 needles [85].	48
Figure 3-8: contour maps for 4-needle model at t = 60 sections [85].	49
Figure 3-9: the motion process of drug molecules.	51
Figure 3-10: the number of particles that has a depth beyond 2000 um in the 2D model.	54
Figure 3-11: initial condition of 3D microneedle simulation.	55
Figure 3-12: 20 seconds of 3D microneedle simulation.	55

Figure 3-13: 40 seconds of 3-D microneedle simulation.....	56
Figure 3-14: 60 seconds of 3D microneedle simulation.....	56
Figure 3-15: 60 secs cross-section of a 3-D microneedle simulation.....	57
Figure 3-16: the number of particles pass the fat layer of a 3D microneedle simulation.....	58
Figure 4-1: build grid index number [87].....	68
Figure 4-2: the repulsive boundary condition [27].....	74
Figure 4-3: the periodic boundary condition [27].....	75
Figure 4-4: the vertical perspective of erythrocyte.....	76
Figure 4-5: The horizontal perspective of erythrocyte.....	77
Figure 4-6: initial condition of the 25% cross-section stenosis blood vessel model.....	77
Figure 4-7: initial condition of the 75% cross-section stenosis blood vessel model.....	78
Figure 4-8: erythrocytes in 25% cross-section stenosis blood vessel model.....	79
Figure 4-9: erythrocytes in 75% cross-section stenosis blood vessel model.....	79
Figure 4-10: cross-section of 75% stenosis blood vessel model.....	80
Figure 4-11: pulsatile flow through the 75 % axisymmetric stenosis [88].....	81
Figure 4-12: human normal blood pressure range [89].....	81
Figure 4-13: pressure of 75% cross-section stenosis blood vessel model.....	82
Figure 4-14: peak pressure of the 75% cross-section stenosis blood vessel model.....	83

LIST OF TABLES

Table 3-1: reference parameters of simulations.....	33
--	----

NOMENCLATURE

Ω domain of integration

C concentration

$W(x)$ kernel function

h smoothing length

μ dynamic viscosity coefficient

τ viscous stress tensor

ε strain rate tensor

c velocity of sound

J diffusion flux

σ total stress tensor

\mathbf{u} velocity

$\nabla \mathbf{u}$ Gradient (u_x, u_y, u_z)

$\nabla \cdot \mathbf{u}$ Divergence $u_x + v_y + w_z$

$\nabla \times \mathbf{u}$ Curl of Vector Field \mathbf{u}

\mathbf{n} Unit Normal Vector

Δt Time Step Size

N number of particles

r distance

α, β direction of coordinates

i, j Specific particles

ACKNOWLEDGMENTS

First and foremost, I want to thank my advisor Dr. Don Liu. It has been an honor to be his Ph.D. student. I appreciate all his contributions of time, ideas, and funding to make my Ph.D. experience productive and stimulating. His enthusiasm for academic research inspired me to overcome difficulties, even during tough times in pursuing my Ph.D.

Special thanks to my committee: Dr. Weizhong Dai, Dr. Katie A. Evans, Dr. Box Leangsuksun, and Dr. Songming Hou, as well as all others in COES of Louisiana Tech University for their precious advice and kind help.

My time at Louisiana Tech University was made enjoyable in large part due to the many friends and groups that became a part of my life. I am very grateful to my beloved families for their sacrifice and their love. They have supported me throughout these years. I also want to thank all my colleagues and friends: Haibo Zhang, Yifan Wang, Zhen Li, and Huali Ye, whom I have been working with closely and have built a deep friendship. I want to thank Dr. Guirong Liu and Dr. Moubin Liu whose research results in my dissertation.

My Ph.D. study is supported by grants from Dr. Don Liu from the National Science Foundation. The computational resources were provided by Louisiana Optical Network Initiative, and High-Performance Computing at Louisiana State University.

CHAPTER 1

INTRODUCTION

1.1 Motivation and Background

Fluid mechanics is a branch of mechanics that plays an important role in scientific research. Same as the other disciplines, fluid mechanics is developed by theoretical analysis and experimental research. Theoretical analysis means to find the quantitative results of the problem by the mathematical method. In some extreme condition, it is hard to build experimental model. Only a few problems could find the result by experimental research. Computational Fluid Dynamics (CFD) was developed to make up for this deficiency.

CFD has been studied in all fields of fluid mechanics. The most commonly used numerical methods are finite difference method, finite element method, and the particle method. The finite difference method has been widely used in fluid mechanics. In recent years, for finite element method, there have been quite a few applications in dealing with low-speed fluids, and it is still rapidly developing. Taking the finite element method as an example, since this method was put forward around the 1950s, the finite element method has become one of the most important and indispensable tools in engineering analysis and calculation. At present, people have successfully developed a large number of the finite element commercial software package and has been widely used in engineering analysis. One of the most salient features of the finite element is the use of a pre-defined

grid to discretize a continuum of infinite degrees of freedom into a set of units of finite degrees of freedom. In this way, it is possible to obtain an approximate solution to a complex problem. However, due to the use of the pre-defined mesh, the finite element method becomes difficult to solve for some specific engineering problems. The weaknesses of the finite element method is when applying a finite element analysis to a problem, it is often necessary to focus on the division of the grid.

Finite elements hard to deal with some complex issues include large deformation problems; dynamic crack propagation problems; high-velocity impact and geometric distortion problems; fission material problems; metal forming problems; multi-phase transformation problems, and so on. In order to solve these problems by FEM, the grids need to be re-divided every time step. However, re-divided grids every time step will increase the calculation time significantly. The shortcomings of the finite element method come from the use of its pre-defined grid. To completely solve these issues, we should avoid applying a fixed grid before we start the calculation. Therefore, the idea of a mesh-free method has been proposed and developed rapidly in recent years.

At present, the research on mesh-free method has become one of the hottest research fields in computational mechanics. The mesh-free method is a numerical method that does not require a well-defined mesh when building discrete system equations. Because the united elements are no longer used in mesh-free methods to separate problem domains, the problems mentioned above are naturally solved. Compared with the finite element method, mesh-free methods have been successfully applied to large deformation problems, dynamic crack propagation in metal forming problems, high-velocity impact problems, and penetration problems.

This paper introduces the basic principles, related formulas and calculation techniques of smoothing particle hydrodynamics (SPH) and elaborates the entire calculation process of SPH. Based on the advantages mentioned above, SPH is easily applied to the medical and biological engineering field. The article describes how to establish two-dimensional and three-dimensional microneedle models, demonstrates the simulation results, and proves the feasibility of microneedles in medical injection from the perspective of theory and simulation. A thrombosis model was also established in the article. By changing the size of the thrombus and the viscosity of the blood, the effect of thrombus on the blood flow in the blood vessels was studied. Thrombosis is often the culprit of cardiovascular and cerebrovascular diseases. Today, with the increasing severity of cardiovascular and cerebrovascular diseases, constructing effective models of blood vessels and thrombi have great significance for the study and treatment of cardiovascular and cerebrovascular diseases.

1.2 Background and applications of SPH method

SPH method is widely used in CFD. Some applications of the SPH method are the following:

1. Astrophysical problems: As an adaptive Lagrangian method, the smoothed particle hydrodynamics was originally proposed to solve astrophysical problems in three-dimensional free space. Lucy [1] simulated the fission of the protostar using the SPH method. Gingold and Monaghan [2] studied the rotation and oscillation of a three-dimensional asymmetric spherical polyhedra. Later, the SPH method was also applied to the numerical study of collisions between the Gemini and the planet, the formation and collapse of

galaxies, the development of the fluctuations of gas and dark matter in the expanding universe, and the evolution of the universe problem [3].

2. Incompressible flow problem: any kind of incompressible fluid can theoretically be considered as a weakly compressible fluid. Therefore, in the SPH method, the state equation of the weakly compressible fluid is usually used to simulate the dynamic behavior of the incompressible fluid [4]. The SPH model of artificially compressible fluids is now widely used to simulate dam-break flow, wave mechanics (wave generation, propagation, and wave breaking; wave impact on shore and shore structures; and interaction of waves with rivers and ocean structures) [5], Marine mechanics, coastal and river hydrodynamics and other fields. Monaghan simulated the problems of dam-breaking flow, generation and propagation of solitary waves, and multiphase flow [4]. Shao uses a modified SPH model to simulate the dynamic behavior of near-shore solitary waves [6]. Gomez Gesteira and Dalrymple studied the impact of water waves on high-rise buildings and the phenomenon of breaking waves. Gotoh *et al.* used the SPH turbulence model to simulate wave interactions [7]. Yim studied the problem of water waves caused by vertical plungers. Cleary and Prakash studied the feasibility of the SPH method to simulate a tsunami. Liang *et al.* used the SPH method to simulate and study the design effect of the anti-tsunami housing [8]. Zheng *et al.* used the sub-mass point turbulence model to simulate the dam-breaking flow problem and the problem of solitary wave climbing flow in the nearshore [9].

3. High-velocity impact and penetration problems: High-velocity impact and penetration are typical problems of high-velocity deformation and failure of elasto-plastic materials [10]. In the process of high-velocity impact, when the elasto-plastic material is subjected to a strong impact load, the solid material will be extremely deformed in a very short time [11]. During the penetration process, solid materials may even be destroyed and become "scattered" everywhere in the debris. High-velocity impact and penetration problems involve moving boundaries and moving material interfaces. The traditional finite element method, finite difference method, and finite volume method are difficult to deal with the problem of grid distortion caused by large deformations and high-velocity movement of the material interface. As a pure Lagrangian mesh-free method, the smoothed particle hydrodynamics method can handle these problems easily. Libersky [12] and Randles [13] first applied the SPH method to study high-velocity impact and penetration problems, including HVI, fractures, and cracking. Attane *et al.* coupled the SPH method with the transient dynamics FEM program PRONOTO to perform impact and armor penetration studies. Zhang Hongtao and others used the SPH and FEM coupling technology in the PAM-CRASH software to analyze the bird's front wing collision problem [8]. Zhang Gangming *et al.* presented the discrete process of the continuum mechanics conservation equation in the two-dimensional axisymmetric problem and the SPH discretization scheme and performed a series of high-speed collision simulations. Wang Fang *et al.* used the SPH method to simulate the hypervelocity impact of space debris [14].

4. Explosion impact problem: An important application of the SPH method is the explosion impact from high energy explosive (HE) explosions. When high-energy explosives explode, they generate high-pressure gas, which involves problems such as large deformation, high non-uniformity, interface of moving substances, and changes in free surface. Traditional grid-based finite element method is difficult to carry out accurate and effective numerical simulation analysis of these problems [15]. Swegle and Attaway used the SPH method combined with the finite element to simulate the underwater explosion, and mainly studied the pulsation characteristics of the generated bubbles [16]. Alia and Souli *et al.* used a multi-substance SPH equation to simulate the explosion process. Liu *et al.* used SPH methods to conduct a series of studies on the detonation of high performance explosives, explosive gas expansion, underwater explosions, and the enhancement and attenuation of explosive effects [17].
5. Other applications are magnetic fluid dynamics, elastomer fracture, metal cutting, geotechnical engineering, casting molding, water curtain protection, bio-nano engineering, environmental engineering, and pharmaceutical engineering.

1.3 Outline of Dissertation

This dissertation mainly talks about basic principle of particle methods, especially for SPH method. This article covers almost all aspects of the SPH method, which comprehensively describes the theoretical basis and formula derivation of the SPH method and uses the SPH method to simulate two complex medical problems.

Chapter 1 introduces the motivation and some overall background knowledge of this research work. The research goal and the structure of this dissertation are indicated. In addition, main applications of SPH are introduced in the first chapter and describe details about current development condition about applications in different areas: astrophysical problems, incompressible flow problem, high-velocity impact and penetration problems, explosion impact problem, and some other complex engineering problems.

Chapter 2 gives a literature review covering the background required for SPH method, which includes the basic idea of SPH method, how to extend a simple concept to a complex theory and apply to numerical simulation. In Chapter 2, I also discuss kernel approximation and particles approximation, and how to apply them to the calculations. Base on approximation steps, we could solve the Lagrangian Navi-stocks equation: mass equation, momentum equation and energy equation. In addition, some other techniques are also introduced in this chapter, such as selection of viscosity term, boundary condition and time step algorithms, and so on.

Chapter 3 gives two three-dimensions and three dimensions microneedle simulation by SPH. In order to illustrate correctness of the simulation results, this project uses a high order continuous method, SEM, and a low order discrete method, the SPH, to investigate this new drug delivery system. The concentration of whole computational domain demonstrates the microneedle could replace traditional needle to deliver drug into the blood circulation system.

Chapter 4 describes the process of modeling of thrombus based on medical theory and numerical simulation method. A plenty of new techniques are added in this vessel

thrombus simulations. Generating animation and plot of a cross-section of blood fluid demonstrates the pressure change and velocity change in different models with small thrombus and large thrombus and compare the results of high fidelity thrombus simulation with other researchers' and realistic data.

Chapter 5 concludes the results of the dissertation and recommends some future works, indicate some new challenges of particle method, and predicts new development direction of particle method.

CHAPTER 2

LITERATURE REVIEW

The SPH method is a mesh-free method which performs simulations by solving partial differential equations. There are two main steps: kernel function approximation and particle approximation. First, SPH discretizes the computational domain of partial differential equations. Second, an approximate function is used to represent an arbitrary point of the field function and its derivative. After these two steps, we could achieve physical parameters by kernel function approximation and particle approximation steps.

2.1 The basic idea of the SPH method

The basic idea of the SPH method can be briefly described as follows:

1. The computational domain of the problem is represented by a series of randomly distributed particles. There is no need to divide the computational domain into any meshes, and no connection between particles is required.
2. Apply integral function to approximate the field function.
3. Approximate the integration of kernel Function in the domain by particle approximation.
4. The particle approximation process must be performed in each time step and is not affected by the random distribution of the particle. That is why the SPH method can handle the problem of extreme deformation.

5. Apply the particle approximation to the all relevant terms of the field function in partial differential equations, a series of time-dependent discrete forms of ordinary differential equations can be achieved.
6. Using the explicit integration method to solve ordinary differential equations, we can calculate the value of variables over time.

2.2 Kernel approximation and particles approximation of SPH

Interpolation approximation is the core idea of the SPH method. The SPH equation is usually structured in two key steps. The first step is to approximate the field function using the kernel function. The second step is a particle approximation process that discretizes the integral equation.

2.2.1 Kernel approximation

In the SPH method, integral expression of function $f(x)$ at point x can be written as:

$$f(x) = \int_{\Omega} f(x') \delta(x-x') dx' \quad \text{Eq. 2-1}$$

where x is position vector, f is a function of position vector x , $\delta(x-x')$ is Dirac delta function, Ω integral area of x :

$$\delta(x-x') = \begin{cases} \infty & x = x' \\ 0 & x \neq x' \end{cases} \quad \text{Eq. 2-2}$$

If we use kernel function $W(x)$ to replace Dirac delta function, the integration of $f(x)$ could be written as:

$$f(x) \approx \int_{\Omega} f(x') W(x-x', h) dx' \quad \text{Eq. 2-3}$$

Where Ω is the domain, h is the smoothing length, W is the kernel function or smoothing function. It means we extend the integration area from one point to a circle for 2D

problems and a sphere for 3D problems. If we extend the integration area, problems could be solved by numerical calculation.

2.2.2 Kernel approximation of derivatives

From **Eq. 2-3**, spacial derivative of $f(x)$ could be obtained:

$$\langle \nabla f(x) \rangle = \int_{\Omega} \nabla f(x') W(x-x') dx' \quad \text{Eq. 2-4}$$

Change the right side of equation:

$$[\nabla f(x')] W(x-x', h) = \nabla [f(x') W(x-x', h)] - f(x') \cdot \nabla W(x-x', h) \quad \text{Eq. 2-5}$$

Substituting **Eq. 2-5** into **Eq. 2-4** :

$$\langle \nabla f(x) \rangle = \int_{\Omega} \nabla [f(x') W(x-x', h)] dx' - \int_{\Omega} f(x') \cdot \nabla W(x-x', h) dx' \quad \text{Eq. 2-6}$$

Apply the divergence theorem to the first term on the right side of the equation, and we can obtain the following result:

$$\int_{\Omega} \nabla [f(x') W(x-x', h)] dx' = \int_s f(x') W(x-x', h) \cdot n dS \quad \text{Eq. 2-7}$$

n is a unit vector perpendicular to surface S .

Use the weight function to represent the field function. This step we called the kernel function approximation. Since the kernel function $W(x-x')$ has the support domain, when the support domain is inside of the problem domain, the integral surface term on the right side of the equation becomes zero. If the support domain and the problem domain are interleaved, integration area of the smooth function is truncated by the

boundary of the computation domain. At this time, the integral surface term will no longer be zero. In the case of the support domain and problem domain interleaving, it is necessary to use numerical methods to correct the effect of the boundary influence so that the integral surface term is zero [18].

If points in the support domain which are also in the problem domain, **Eq. 2-7** can be written as:

$$\langle \nabla f(x) \rangle = - \int_{\Omega} f(x') \cdot \nabla W(x - x', h) dx' \quad \text{Eq. 2-8}$$

2.2.3 Particles approximation

In the SPH method, the state of the system is described by a finite number of particles that contain their own physical properties (such as density, pressure, internal energy, velocity, etc.), and particles move and adhere to the governing equation.

According to the basic principle of the SPH method, the solution is represented by a finite number of particles, SPH's continuous integral format can be converted into a discretized format for summation of all particles in the support domain. The summation of particles is always called particle approximation in the SPH related literature. **Figure 2-1** indicates the particles approximation in the support domain.

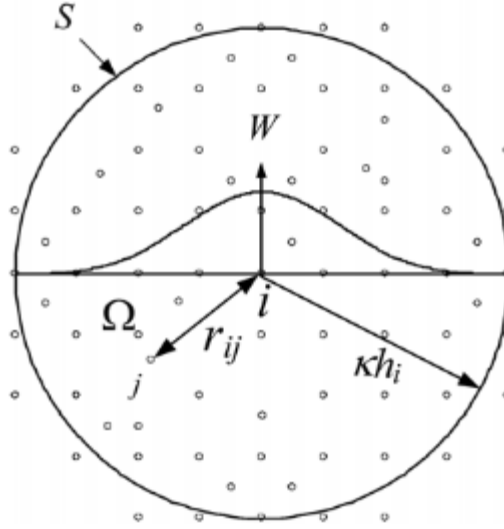


Figure 2-1: particles approximation in the support domain [4].

The process of particle approximation is as follows: if we use finite volume ΔV_j to replace integration of dx' at point x , m_j could be obtained as:

$$m_j = \Delta V_j \rho_j \quad \text{Eq. 2-9}$$

Where ρ_j is the density of point j , $j=1,2,3,4\dots N$, N is the total number of particles in the support domain of particle j . The continuous integral form of $f(x)$ can be written as a discretized particle approximation:

$$\begin{aligned} \langle f(x) \rangle &= \int_{\Omega} f(x') W(x-x', h) dx' & \text{Eq. 2-10} \\ &\cong \sum_{j=1}^N f(x_j) W(x-x_j, h) \Delta V_j \\ &= \sum_{j=1}^N f(x_j) W(x-x_j, h) \frac{1}{\rho} (m_j) \end{aligned}$$

The particle approximation of the function at particle i can be written as:

$$\langle f(x_i) \rangle = \sum_{j=1}^N \frac{m_j}{\rho_j} f(x_j) W_{ij} \quad \text{Eq. 2-11}$$

$$W_{ij} = W(x_i - x_j, h) = W(|x_i - x_j|, h) = W(R_{ij}, h) \quad \text{Eq. 2-12}$$

Where $R_{ij}=r_{ij}/h$ is the relative distance between particle i and particle j , r_{ij} is the distance between two particles. The function value at any point in computation domain could be achieved by the kernel function.

The particle approximation of the function's spatial derivatives can be written as:

$$\langle \nabla f(x) \rangle = - \sum_{j=1}^N \frac{m_j}{\rho_j} f(x_j) \nabla W(x - x_j, h) \quad \text{Eq. 2-13}$$

The gradient function ∇W is related to the particle j , and the final form of particle approximation can be written as:

$$\langle \nabla f(x_i) \rangle = - \sum_{j=1}^N \frac{m_j}{\rho_j} f(x_j) \nabla W_{ij} \quad \text{Eq. 2-14}$$

$$\nabla W_{ij} = \frac{x_i - x_j}{r_{ij}} \frac{\partial W_{ij}}{\partial r_{ij}} = \frac{x_{ij}}{r_{ij}} \frac{\partial W_{ij}}{\partial r_{ij}} \quad \text{Eq. 2-15}$$

SPH method is widely used in CFD by quite a few researchers because particles in the SPH method not only interpolates but also carry materials density and mass in the particles approximation of formulas. This advantage is more significant for large deformation problems.

2.3 Kernel function

2.3.1 Characteristics of kernel function

The kernel function is an essential part in SPH method because it determines both the form of the function approximation and the size of the particle support domain. It also

determines the consistency and accuracy of the kernel approximation and the particle approximation. The SPH smooth function should generally satisfy the following conditions:

1. The smoothing function must be normalized over its support domain (Unity):

$$\int_{\Omega} W(x-x', h) dx = 1 \quad \text{Eq. 2-16}$$

This normalization property ensures that the integral of the smoothing function over the support domain to be unity.

2. The smoothing function should be compactly supported (Compact support):

$$W(x-x', h) = 0 \text{ when } |x-x'| > kh \quad \text{Eq. 2-17}$$

The dimension of the compact support is defined by the smoothing length h and a scaling factor k , where h is the smoothing length, and determining the spread of the specified smoothing function $|x-x'| \leq kh$ defines the support domain of the particle at point x . This compact support property transforms an SPH approximation from a global operation to local operation.

3. $W(x-x') \geq 0$, 0 for any point at x within the support domain of the particle at Particle x . This property indicates that the kernel function should be non-negative in the support domain. It is not necessary as a convergent condition mathematically, but it is essential to ensure a stable representation of some physical properties. Some kernel functions used in some literature are negative in parts of the support domain.
4. The kernel function value for a particle should be decreasing with the increase of the distance away from the particle monotonically. This property depends

on the physical aspect in that a nearer particle should have a bigger effect on the particle selected.

5. The smoothing function should satisfy the Dirac delta function property when the smoothing length trends zero :

$$\lim_{h \rightarrow 0} W(x - x', h) = \delta(x - x') \quad \text{Eq. 2-18}$$

This feature ensures that as the smoothing length tends to be zero, the approximation value approaches the function value, i.e. $\langle f(x) \rangle = f(x)$.

6. The kernel function should be an even function (Symmetric property). This rule indicates that particles have distance but don't have same positions should have the same influence on a selected particle.

7. The kernel function should be sufficiently smooth (Smoothness). This feature aims to obtain better approximation accuracy.

2.3.2 Kernel functions in the literature

2.3.2.1 The bell-shaped function

Lucy [1] first proposed a bell-shaped function as the kernel function in early SPH paper:

$$W(x - x', h) = W(R, h) = \alpha_d \begin{cases} (1 + 3R)(1 - R)^3 & R \leq 1 \\ 0 & R > 1 \end{cases} \quad \text{Eq. 2-19}$$

For dealing with different dimensional problems, α_d could have different values.

Corresponding to one-dimensional, two-dimensional and three-dimensional problems, should equal $5/4h$, $5/\pi h^2$, $105/16\pi h^3$, r is the distance between two particles.

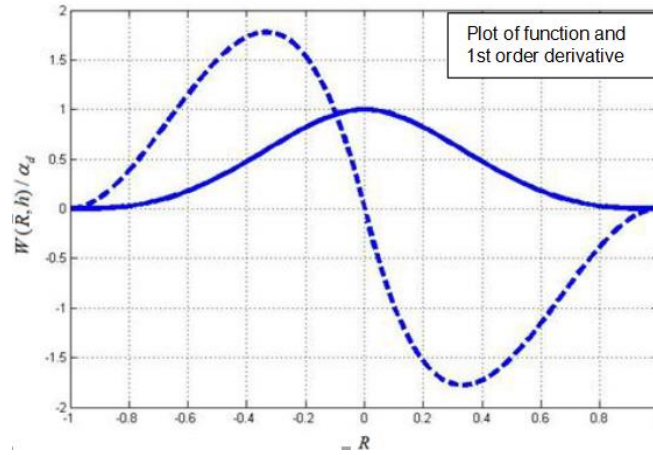


Figure 2-2: bellloid kernel function and its first derivative curve [15].

2.3.2.2 Gaussian kernel function

Monaghan [5] first proposed Gaussian kernel function:

$$W(x - x', h) = W(R, h) = \alpha_d e^{-R^2} \quad \text{Eq. 2-20}$$

For one-dimensional, two-dimensional and three-dimensional problems, α_d should equal $1/\pi^{1/2}h$, $1/\pi h^2$, $1/\pi^{3/2}h^3$. Due to Gaussian type kernel function's high stability and high precision, it is an excellent choice for the simulation of disordered particle distribution. However, if using the Gaussian kernel function in simulation requires a large amount of computation. Because the kernel function needs long distances tend to zero, especially for higher order derivatives of smooth functions. **Figure 2-3** shows Gaussian kernel function and its first derivative curve [15].

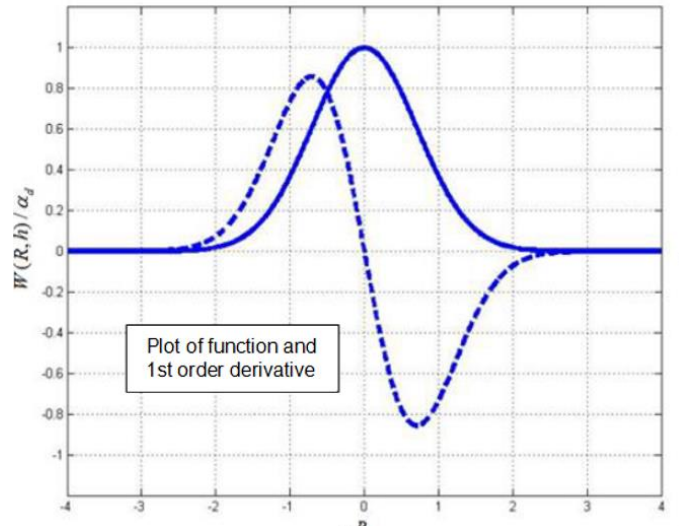


Figure 2-3: Gaussian kernel function and its first derivative curve [15].

2.3.2.3 Cubic spline and B-spline kernel function

Cubic spline kernel function [5]:

$$W(r, h) = \alpha_d \begin{cases} 1 - \frac{3}{2}q^2 + \frac{3}{4}q^3 & 0 \leq q \leq 1 \\ \frac{1}{4}(2-q)^3 & 1 \leq q \leq 2 \\ 0 & q \geq 2 \end{cases} \quad \text{Eq. 2-21}$$

α_d equals to $10/7 \pi h^2$ in 2D problem, and in 3D problem α_d equals to $1/\pi h^3$.

Based on the cubic spline smooth function, the B-spline kernel function is proposed by Monaghan and Lattanzi [66]:

$$W(R, h) = \begin{cases} \frac{2}{3} - R^2 + \frac{1}{2}R^3 & 0 \leq R < 1 \\ \frac{1}{6}(2-R)^3 & 1 \leq R < 2 \\ 0 & R \geq 2 \end{cases} \quad \text{Eq. 2-22}$$

For one-dimensional, two-dimensional and three-dimensional problems, α_d

should equal to $1/h$, $15/7\pi h^2$, $3/2\pi h^3$. The cubic spline is the most widely used kernel function in the existing SPH literature. The cubic spline kernel function is similar to the Gaussian kernel function; the support domain is narrow, too. When the distance between two particles exceeds $2h$, the interaction between particles disappears and this property reduces a lot of calculations [22]. Because the second derivative of the cubic spline function is a piecewise linear function, the stability of the cubic spline function is worse than other higher-order kernel functions. **Figure 2-4** indicates plot of B-spline kernel function and its 1st order derivative curve [15].

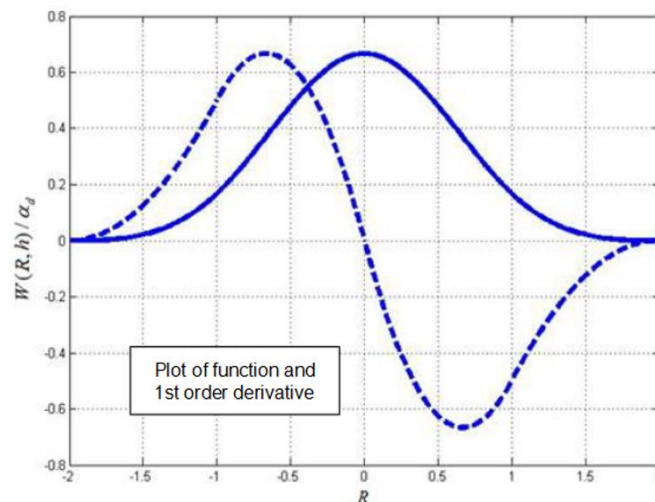


Figure 2-4: plot of B-spline kernel function and its 1st order derivative curve [15].

2.3.2.4 *The fourth and fifth spline kernel functions*

The fourth and fifth spline smoothing functions are closer to the Gaussian kernel than the cubic spline functions and have better stability.

$$W(R, h) = \alpha_d \begin{cases} (2.5 + R)^2 - 5(1.5 + R)^4 + 10(0.5 + R)^4 & 0 \leq R \leq 0.5 \\ (2.5 + R)^2 - 5(1.5 + R)^4 & 0.5 \leq R \leq 1.5 \\ (2.5 + R)^2 & 1.5 \leq R \leq 2.5 \\ 0 & 2.5 \leq R \end{cases} \quad \text{Eq. 2-23}$$

For one-dimensional, α_d should equal to $1/24h$ [27].

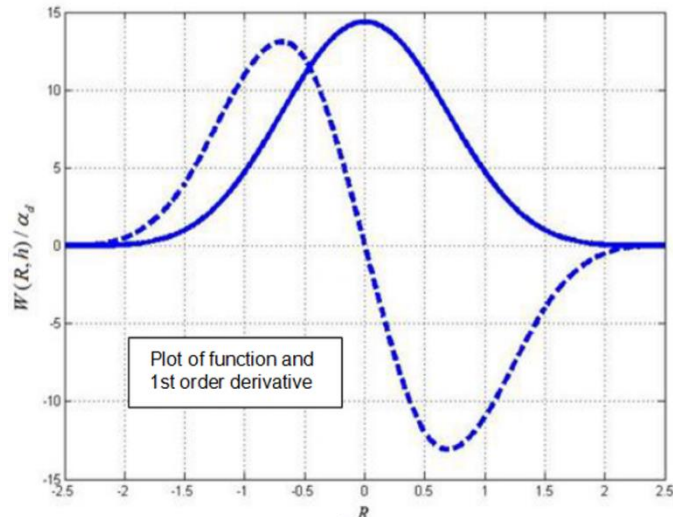


Figure 2-5: the fourth spline kernel function and its 1st order derivative curve [15].

The fifth spline smoothing function:

$$W(R, h) = \alpha_d \begin{cases} (3 - R)^5 - 5(2 - R)^5 + 15(1 - R)^4 & 0 \leq R \leq 1 \\ (3 - R)^5 - 5(2 - R)^5 & 1 \leq R \leq 2 \\ (3 - R)^5 & 2 \leq R \leq 3 \\ 0 & 3 \leq R \end{cases} \quad \text{Eq. 2-24}$$

For one-dimensional, two-dimensional and three-dimensional problems, α_d should equal to $120/h$, $7/478\pi h^2$, $3/359\pi h^3$. The plot of fifth kernel function and its 1st order derivative curve [15] shows in **Figure 2-6**.

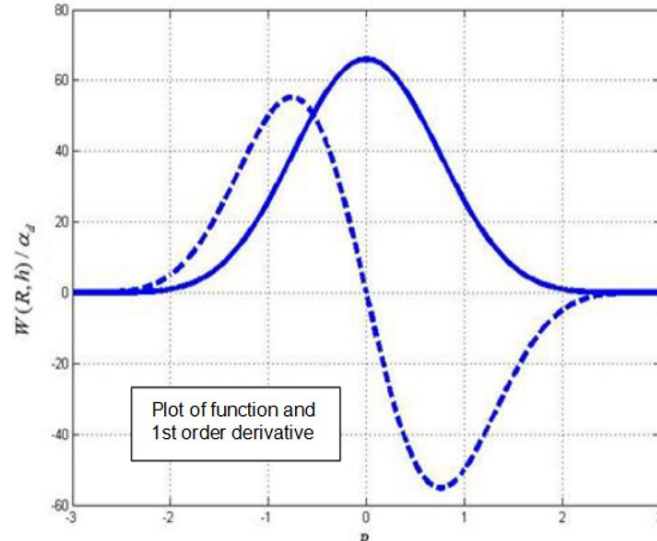


Figure 2-6: plot of fifth kernel function and its 1st order derivative [15].

2.3.3 Approximate accuracy of SPH method

SPH is usually considered as a second-order precision method. Using the Taylor series to expand $f(x)$ in x , **Eq. 2-3** can be written as:

$$\begin{aligned} \langle f(x) \rangle &= \int_{\Omega} [f(x) + f'(x)(x'-x) + r((x'-x)^2)] \times W(x-x', h) dx' \\ &= f(x) \int_{\Omega} W(x-x') dx' + f'(x) \int_{\Omega} (x'-x) W(x-x', h) dx' + r(h^2) \end{aligned}$$

Eq. 2-25

Because $W(x-x', h)$ is an even function, Eq. 2-25 is an odd function. The integration of function is equal to 0:

$$\int_{\Omega} (x'-x) W(x-x', h) dx' = 0$$

Eq. 2-26

$$\langle f(x) \rangle = f(x) + r(h^2)$$

Eq. 2-27

Although the kernel function approximation has second-order accuracy, the discretized SPH approximation has second-order accuracy and must satisfy the following conditions:

$$\sum_{j=1}^N \frac{m_j}{\rho_j} W(x - x_j, h) = 1 \quad \text{Eq. 2-28}$$

$$\sum_{j=1}^N \frac{m_j}{\rho_j} (x - x_j) W(x - x_j, h) = 0 \quad \text{Eq. 2-29}$$

Eq. 2-26 may not be true for all cases. If the kernel function's support domain and the problem domain are interleaved, integration area of the smooth function is truncated by the boundary of the problem domain [31]. At this time, the surface integral term will no longer be zero. In this condition, SPH method does not have second-order accuracy. In another case, due to the particles in the support domain being non-uniformly distributed, summation of particles cannot exactly satisfy the above conditions [32].

2.4 Consistency of SPH method

In theory, any numerical method should describe the physical problem as realistically as possible. The SPH method can completely use the continuity analysis theory of finite element method to analyze continuous and discrete forms of numerical formats. If an approximate form of a meshless particle method is capable of accurately regenerating a k^{th} polynomial, this approximate form has C^k order continuity.

2.4.1 Consistency in kernel approximation

If $f(x)$ is sufficiently smooth, the applying Taylor series expansion of $f(x')$ gives us:

$$\begin{aligned}
 f(x') &= f(x) + f'(x)(x' - x) + \frac{1}{2} f''(x)(x' - x)^2 + \dots & \text{Eq. 2-30} \\
 &= \sum_{k=0}^n \frac{(-1)^k h^k f^{(k)}(x)}{k!} \left(\frac{x - x'}{h} \right)^k + r_n \left(\frac{x - x'}{h} \right)
 \end{aligned}$$

Substituting **Eq. 2-27** into **Eq. 2-24**:

$$\langle f(x) \rangle = \sum_{k=0}^n A_k f^{(k)}(x) + r_n \left(\frac{x - x'}{h} \right) \quad \text{Eq. 2-31}$$

$$A_k = \frac{(-1)^k}{k!} \int_{\Omega} (x - x')^k W(x - x', h) dx' \quad \text{Eq. 2-32}$$

Consider the SPH kernel function approximate to the n^{th} order of the field function, then the following equations can be obtained:

$$\left. \begin{aligned}
 M_0 &= \int_{\Omega} W(x - x', h) dx' = 1 \\
 M_1 &= \int_{\Omega} (x - x') W(x - x', h) dx' = 0 \\
 M_2 &= \int_{\Omega} (x - x')^2 W(x - x', h) dx' = 0 \\
 &\vdots \\
 M_n &= \int_{\Omega} (x - x')^n W(x - x', h) dx' = 0
 \end{aligned} \right\} \quad \text{Eq. 2-33}$$

Where M_k is the k -th moments of the kernel function. In other words, any field function kernel approximation has $n+1$ order accuracy [34]. The SPH kernel function must satisfy the continuity condition of a series of integral forms represented by **Eq. 2-32**. These consistency conditions can be used to construct special forms of kernel functions.

2.4.2 Consistency in particles approximation

The particle approximation of **Eq. 2-32** can obtain the corresponding discrete form of SPH particles:

$$\left. \begin{aligned} \sum_{j=1}^N W_{ij} \Delta v_j &= 1 \\ \sum_{j=1}^N (x_i - x_j) W_{ij} \Delta v_j &= 0 \\ &\vdots \\ \sum_{j=1}^N (x_i - x_j)^n W_{ij} \Delta v_j &= 0 \end{aligned} \right\} \text{Eq. 2-34}$$

Eq. 2-32 gives the particle continuity conditions. If the constructed SPH particle discrete format satisfies **Eq. 2-32**, this SPH particle discretization format can accurately approximate any field function to $n+1$ order accuracy. Then, particle approximation has n -order continuity [34].

In some special conditions, the continuity condition of the integral form and the continuity condition of the discrete form may not be established at the same time. In addition to the particle approximation format, the value of the smooth length, the smooth function selected, the distribution of the particles, etc. may affect the accuracy of the calculation [35]. The first and second formulas in **Eq. 2-32** are the regularization conditions and symmetry conditions that must be satisfied by the discrete form of the kernel function. For the one-dimensional case, if the particles are regularly distributed in a symmetric form of a smooth function, the smooth length is the particle spacing, and for internal particles, the regularization conditions and symmetry conditions of the discrete form are established. So SPH particles approximation has second-order accuracy. On the contrary, if the initial particles in the support domain are irregularly distributed, the discrete form of the particles may not be able to reach the above conditions accurately. Therefore, the accuracy of the SPH method is determined by different formats of the kernel approximation and the particle approximation [52].

2.5 SPH formulations for Navier-Stokes(N-S) equations

Using the Lagrangian description, the governing equation of continuum mechanics includes the following series of equations:

Mass conservation equation [4]:

$$\frac{d\rho}{dt} = -\rho \nabla \cdot u \quad \text{Eq. 2-35}$$

Momentum conservation equation [4], [90]:

$$\frac{du_\alpha}{dt} = - \left(\frac{\nabla p}{\rho} \right)_\alpha \quad \text{Eq. 2-36}$$

Energy conservation equation [4], [90]:

$$\frac{de}{dt} = - \frac{p}{\rho} \nabla \cdot u \quad \text{Eq. 2-37}$$

ρ is the fluid density, u is the fluid velocity, p is the pressure, α is the direction.

2.5.1 Particles approximation of density

In the SPH method, the particle approximation of the density is very important because the density determines the distribution of the particles and the change in the smooth length. At present, there are two approximate methods of density in the SPH method. One is the density summation method. This method directly applies the SPH approximation to the density. For given particle i , the density of the particle obtained by the density summation method:

$$\rho_i = \sum_j m_j W_{ij} \quad \text{Eq. 2-38}$$

Eq. 2-37 [4] describes the density of particles; i can be approximated by a weighted average of the densities of all the particles in its support domain. Using **Eq. 2-**

37 as the SPH approximation of density, the discrete equation strictly satisfies the law of conservation of mass [36].

The second is the continuous density method, which is the expression of the solution density obtained from the SPH approximation of the continuous equation. For different transformation methods of the right term of the continuous equation, different density approximation equations can be obtained [4]:

$$\frac{d\rho_i}{dt} = -\rho_i \sum_{j=1}^N \frac{m_j}{\rho_j} u_j^\beta \frac{\partial W_{ij}}{\partial x_i^\beta} \quad \text{Eq. 2-39}$$

The expression of particle approximation with unit gradient:

$$\nabla 1 = \int 1 \cdot \nabla W(x - x', h) dx' = \sum_{j=1}^N \frac{m_j}{\rho_j} \cdot \frac{\partial W_{ij}}{\partial x_i^\beta} = 0 \quad \text{Eq. 2-40}$$

Because:

$$\rho_i \sum_{j=1}^N \frac{m_j}{\rho_j} u_j^\beta \frac{\partial W_{ij}}{\partial x_i^\beta} = \rho_i u_j^\beta \left(\sum_{j=1}^N \frac{m_j}{\rho_j} \frac{\partial W_{ij}}{\partial x_i^\beta} \right) \quad \text{Eq. 2-41}$$

Eq. 2-39 could be written as:

$$\frac{d\rho_i}{dt} = \rho_i \sum_{j=1}^N \frac{m_j}{\rho_j} u_{ij}^\beta \frac{\partial W_{ij}}{\partial x_i^\beta} \quad \text{Eq. 2-42}$$

Eq. 2-42 introduces the difference of velocity in discrete particle approximation; it is because it calculates the relative velocities between the particles in the support domain and can use the antisymmetric form of relative velocities to reduce the error caused by particle non-continuity. If the gradient operator is applied to the SPH approximation function, the most commonly used SPH continuity density equation is obtained:

$$\frac{d\rho_i}{dt} = \sum_{j=1}^N m_j u_{ij}^\beta \frac{\partial W_{ij}}{\partial x_i^\beta} \quad \text{Eq. 2-43}$$

The time rate of density relates to the difference of velocity between every particle in the support domain and the center particle. Two different density approximation methods have their own advantages and disadvantages. When the density summation method integrates over the entire problem domain, the quality is precisely conserved because the quality of the entire region is the sum of the particle mass when interpolating the integration. However, in the calculation of the continuous density method, the quality is not accurately conserved. Therefore, when using the summation method, edge effects occur when the particles are close to the boundary. This problem can be solved by setting up virtual particles at the boundary. The boundary effect does not only occur on the boundary of the same kind of media. If the problem has multiple substances, boundary effects also occur on the adjacent boundaries of different substances. Another disadvantage of the summation method is that we must first calculate the density of each particle to get other parameters, which leads to an increase in the amount of calculation. The quality of integrating over the entire problem domain may not necessarily exactly be conserved. Since it calculates other parameters without calculating the density of each particle first and easy to reduce the calculation time [37].

2.5.2 Approximation of momentum equation

For conservation of momentum equation, there are three terms: viscous term, and pressure term, external force term.

The pressure term is:

$$\left(\frac{1}{\rho} \nabla p\right)_i = \frac{1}{\rho_i^2} \sum_j m_j (p_j - p_i) \nabla_i W_{ij} \quad \text{Eq. 2-44}$$

Transform pressure term:

$$\left(\frac{1}{\rho} \nabla p\right)_i = \frac{p}{\rho^2} \nabla \rho + \nabla \left(\frac{p}{\rho}\right) \quad \text{Eq. 2-45}$$

Discrete right side of equation:

$$\begin{aligned} \left(\frac{p}{\rho^2} \nabla \rho + \nabla \left(\frac{p}{\rho}\right)\right)_i &= \frac{p_i}{\rho_i^2} \sum_j \frac{m_j}{\rho_j} \rho_j \nabla_i W_{ij} + \sum_j \frac{m_j}{\rho_j} \frac{p_j}{\rho_j} \nabla_i W_{ij} \\ &= \sum_j m_j \frac{p_i}{\rho_i^2} \nabla_i W_{ij} + \sum_j m_j \frac{p_j}{\rho_j^2} \nabla_i W_{ij} \\ &= \sum_j m_j \left(\frac{p_i}{\rho_i^2} + \frac{p_j}{\rho_j^2}\right) \nabla_i W_{ij} \end{aligned} \quad \text{Eq. 2-46}$$

Substituting into **Eq. 2-46**:

$$\left(\frac{1}{\rho} \nabla p\right)_i = \sum_j m_j \left(\frac{p_i}{\rho_i^2} + \frac{p_j}{\rho_j^2}\right) \nabla_i W_{ij} \quad \text{Eq. 2-47}$$

Studies have shown that this symmetric form reduces errors due to particle inconsistencies.

2.5.3 Approximation of energy equation

In the Navier-Stokes equation, if the stress tensor is decomposed into isotropic pressure and viscous stress, the energy equation can be written as:

$$\frac{de_i}{dt} = -\frac{p}{\rho} \frac{\partial u_i^\beta}{\partial x_i^\beta} + \frac{\mu_i}{2\rho_i} \varepsilon_i^{\alpha\beta} \varepsilon_j^{\alpha\beta} \quad \text{Eq. 2-48}$$

and

$$\begin{aligned}
-\frac{p}{\rho} \frac{\partial u_i^\beta}{\partial x_i^\beta} &= \frac{p}{\rho^2} \left(-\rho \frac{\partial u_i^\beta}{\partial x_i^\beta} \right) = \frac{p}{\rho^2} \frac{d\rho}{dt} \\
-\frac{p}{\rho} \frac{\partial u_i^\beta}{\partial x_i^\beta} &= -\frac{\partial}{\partial x_i^\beta} \left(\frac{p u_i^\beta}{\rho} \right) + \mu_i^\beta \frac{\partial}{\partial x_i^\beta} \left(\frac{p}{\rho} \right)
\end{aligned}
\tag{Eq. 2-49}$$

The following equation could be achieved:

$$-\frac{p}{\rho} \frac{\partial u_i^\beta}{\partial x_i^\beta} = \frac{1}{2} \sum_{j=1}^N m_j \left(\frac{p_i}{\rho_i^2} + \frac{p_j}{\rho_j^2} \right) u_{ij}^\beta \cdot \frac{\partial W_{ij}}{\partial x_i^\beta}
\tag{Eq. 2-50}$$

Use the above equation to approximate the change rate of density:

$$-\frac{p}{\rho} \frac{\partial u_i^\beta}{\partial x_i^\beta} = \frac{p_i}{\rho_i} \sum_{j=1}^N \frac{m_j}{\rho_j} u_{ij}^\beta \cdot \frac{\partial W_{ij}}{\partial x_i^\beta}
\tag{Eq. 2-51}$$

Since there are many different expressions for the approximation of pressure work, there are many options for measuring the internal energy corresponding to the pressure work [42]. In general, the most commonly used calculation formulas have the following two forms:

$$\begin{aligned}
\frac{de_i}{dt} &= \frac{1}{2} \sum_{j=1}^N m_j \left(\frac{p_i}{\rho_i^2} + \frac{p_j}{\rho_j^2} \right) u_{ij}^\beta \cdot \frac{\partial W_{ij}}{\partial x_i^\beta} + \frac{\mu_i}{2\rho_i} \varepsilon_i^{\alpha\beta} \varepsilon_j^{\alpha\beta} \\
\frac{de_i}{dt} &= \frac{1}{2} \sum_{j=1}^N m_j \frac{p_i + p_j}{\rho_i \rho_j} u_{ij}^\beta \cdot \frac{\partial W_{ij}}{\partial x_i^\beta} + \frac{\mu_i}{2\rho_i} \varepsilon_i^{\alpha\beta} \varepsilon_j^{\alpha\beta}
\end{aligned}
\tag{Eq. 2-52}$$

CHAPTER 3

CONTINUOUS AND DISCRETE SIMULATIONS OF MICRO-NEEDLES FOR EPIDERMAL DRUG DELIVERY

As an emerging transdermal drug delivery device, microneedles demonstrate some superior potential and advantages over traditional metallic needles-on-syringes in skin injection and vaccine [1]. However, very few research papers are available. This project uses a high order continuous method, the spectral element method (SEM), and a low order discrete method, the Smoothed Particle Hydrodynamics (SPH), to investigate this new drug delivery system. The incompressible Navier-Stokes equations were solved with SEM under appropriate initial and slip boundary conditions for the transport of medicine inside microneedles of rectangular and circular cross-sections. In addition, Darcy-Brinkman equations and a concentration equation were solved with SEM under appropriate initial and boundary conditions for the infiltration of medicine solution through porous media of dermis tissue once a microneedle enters the skin. Meanwhile, the Lagrangian form of the Navier-Stokes equations were solved with the weighted interpolation approach via numerical integrations without inverting any matrices. Results from the mesh-based SEM and the mesh-free SPH simulations revealed technical details about the processes of delivery of medicine particles through microneedles and diffusion in the skin tissue, and the medicine concentration change with space and time. The

overall effect of medicine delivery under initial concentration and conditions were simulated and the effect of drug delivery were assessed.

3.1 Introduction

Traditional injection uses a syringe to insert liquid into the body. The purpose of medical injection is to pierce the material into the sufficient depth of the skin. This kind of injection needs to use a large number of syringe needles, and according to [61], clients reported that an average of 8.7% of injections employed shared syringe needles. Data from the Coalition for safe Community Needle Disposal showed that in 2011, 13.5 million people in the United States produced 7.8 billion used sharps (needles, syringes, etc.) outside the traditional healthcare, and 1 million to 1.5 million of needles were used for illegal drug injections. Since blood borne infections, like HIV, HBV, and HCV, can be commonly spread by sharing intravenous syringes, a large number of substandard and illegal use of needles compares to the shared rate of 8.7%; the potential spread of these infections cannot be ignored. On the other hand, the application of the micro needle can to a large extent eliminate this from its source.

Micro needles, which are recently developed by the Georgia Institute of Technology and the Centers for Disease Control and Prevention (CDC) [62, 63], are small patches that can be administered by untrained users. Small needles are placed on the patch of about one square centimeter. Instead of asking a nurse for a muscle injection, only with a press of a thumb, this kind of needle can be used for vaccine inoculation and local anesthesia.

In this paper, both the spectral element method and the smoothed particle hydrodynamics method are applied to simulate the models of the micro needle. The

spectral element method used in computational fluid dynamics is explained in [15] and [45]. For spectral element models of the micro needle, the process is divided into two parts, the model of the flow in the micro-needle and the model of the solution flux inside human skin. Incompressible Navier-Stokes equations with slip boundary condition are solved inside the micro needle. The human skin is treated as porous media, so the Darcy-Brinkman equation is solved to simulate this process. At the same time, the output data of the micro needle are taken as the initial conditions of the Darcy-Brinkman model.

The mesh free method for large deformation problems of fluid simulation compared with the traditional grid method has obvious advantages, the traditional method unable to deal with a large deformation problem of fluid, because the local grid deformation is too large and will cause the computation result to distort. This simulation uses the SPH algorithm to simulate the movement of a drug's molecule in the porous medium of the dermis after a single micro needle pierced skin. Micro needle compared with the traditional needle injection has obvious merits. Besides reducing the piercing pain, the drug will penetrate more uniform and faster. Two models illustrate these characteristics. **Table 3-1** shows reference parameters of simulations.

Table 3-1: reference parameters of simulations.

Convection and Diffusion	
Diffusivity Coefficient of Lidocaine, D	$1.38 \times 10^{-8} \text{ m}^2/\text{s}$ [65]
Fluid Flow	
Density of Lidocaine, ρ	$999 \text{ kg}/\text{m}^3$ [66]
Dynamic Viscosity of Lidocaine, η	$0.001 \text{ Pa} \cdot \text{s}$ [67]
Porosity, Φ	0.5 [68]
Intrinsic Permeability of Skin, k	10^{-17} m^2 [69]
Minimum Concentration Required at Nerves	$0.004267 \text{ mol}/\text{m}^3$ [70]
Initial Concentration at output of needle	$42.67 \text{ mol}/\text{m}^3$ [71]

Some of the original data come from students' report [71], and all the parameters shown in Table above are confirmed from their citations.

3.2 Methodology

3.2.1 Discrete Modeling

The Smoothed Particle Hydrodynamics is a weighted interpolation method [72] used to describe the motion of solid, liquid or gas in space with a discrete interpolation. The interpolating function is denoted as $W(r - r', h)$ where h is the radius of the influenced region around position r' . The interpolating function is essentially a probability density function [73].

In this two-dimensional micro needle model, we use fixed points which are randomly distributed to represent the porous media of the dermal layer. Molecules move

into a porous medium dermis, collide with porous media, and disperse in the dermis layer gradually. Human dermal thickness is generally around 2 mm; the model of the porous media thickness is 4 mm; the length of the micro needle is 600 μm ; the base diameter is 400 μm . When the depth of molecular particles is around 2 mm, they have entered the subcutaneous tissue and capillaries, and throughout the blood flow. By measuring the number of particles beyond 2 mm, we can calculate the concentration of the drug molecules in units of blood.

The momentum equation, containing stress tensor σ , in the component form is shown as the following [79]:

$$\frac{dv^a}{dt} = \frac{1}{\rho} \frac{\partial \sigma^{ab}}{\partial x^b} + f^a \quad \text{Eq. 3-1}$$

where a, b stand for Cartesian components, f^a is the body force, and the tensor stress σ^{ab} is consisted of the deviatoric stress S^{ab} and the volumetric stress $P\delta^{ab}$. Since the volumetric stress is easy to calculate, the following equation describes how the change rate of the deviatoric stress occurs:

$$\frac{dS^{ab}}{dt} = 2\mu \left(\dot{\epsilon}^{ab} - \frac{1}{3} \delta^{ab} \dot{\epsilon}^{ab} \right) + S^{ac} \Omega^{bc} + \Omega^{ac} S^{cb} \quad \text{Eq. 3-2}$$

in which Ω^{ab} and $\dot{\epsilon}^{ab}$ are calculated by:

$$\dot{\epsilon}^{ab} = \frac{1}{2} \left(\frac{\partial v^a}{\partial x^b} + \frac{\partial v^b}{\partial x^a} \right) \quad \text{Eq. 3-3}$$

$$\Omega^{ab} = \frac{1}{2} \left(\frac{\partial v^a}{\partial x^b} - \frac{\partial v^b}{\partial x^a} \right) \quad \text{Eq. 3-4}$$

The derivatives of velocity in **Eq. 5-20** and **Eq. 5-21** are calculated according to [80]:

$$\left(\frac{\partial v^a}{\partial x^b}\right)_i = - \sum_j \frac{m_j}{\bar{\rho}_{ij}} (v_i^a - v_j^a) \frac{\partial W_{ij}}{\partial x_i^b} \quad \text{Eq. 3-5}$$

where $\bar{\rho}_{ij} = \frac{\rho_i + \rho_j}{2}$.

The momentum equation for the SPH scheme is:

$$\frac{dv_i^a}{dt} = \sum_j m_j \left(\frac{\sigma_i^{ab}}{\rho_i^2} + \frac{\sigma_j^{ab}}{\rho_j^2} \right) \frac{\partial W_{ij}}{\partial x_i^b} + f^a \quad \text{Eq. 3-6}$$

3.2.1.1 Particles Interaction

Interactions between particles are described with a pair-wise force field similar to the Lennard-Jones potential [80]:

$$\mathbf{f}_{ij} = C_0 \left[\left(\frac{r_0}{|\mathbf{r}_{ij}|} \right)^{p_1} - \left(\frac{r_0}{|\mathbf{r}_{ij}|} \right)^{p_2} \right] \frac{\mathbf{r}_{ij}}{|\mathbf{r}_{ij}|} \quad \text{Eq. 3-7}$$

where $\mathbf{r}_{ij} = \mathbf{r}_i - \mathbf{r}_j$, r_0 is the initial distance between two different particles i and j . In this case, $p_1 = 12$, $p_2 = 6$, C_0 is an adjustable constant.

3.2.1.2 Velocity Evaluation

The motion of the particle i is described in the equation below [82]:

$$\frac{dr_i}{dt} = v_i + \varepsilon \sum_j m_j \left(\frac{v_j - v_i}{\bar{\rho}_{ij}} \right) W_{ij} \quad \text{Eq. 3-8}$$

in which ε ($0 \leq \varepsilon \leq 1$ according to different case) is a factor that averages the velocity of influence.

3.3 Viscosity term

In the SPH method, viscosity is essential for the results of numerical simulations, for different viscous term selections often achieve different numerical simulation results.

Therefore, how to select the proper viscous item is very important. It is necessary to select the proper viscous item according to the simulation model [39].

3.3.1 Artificial viscosity

To simulate the fluid dynamics problem, some special processing is needed to eliminate the non-physical oscillations and the numerical oscillations generated during the calculation. So, artificial viscosity is added into the SPH method. Artificial viscosity is usually added to the pressure term. So far, Monaghan's artificial viscosity is the most widely used in SPH-related literatures. It not only converts kinetic energy into heat energy, but also provides the shock wave surface dissipation in the formulas, and it can prevent non-physical penetration of particles when they are close to each other. The expression is:

$$\Pi_{ij} = \begin{cases} \frac{-\overline{\alpha c_{ab} \mu_{ab}}}{\rho_{ab}} & \mathbf{u}_{ab} \cdot \mathbf{r}_{ab} < 0 \\ 0 & \mathbf{u}_{ab} \cdot \mathbf{r}_{ab} > 0 \end{cases} \quad \text{Eq. 3-9}$$

$$\mathbf{r}_{ab} = \mathbf{r}_a - \mathbf{r}_b \quad \text{Eq. 3-10}$$

$$\mathbf{v}_{ab} = \mathbf{v}_a - \mathbf{v}_b$$

$$\mu_{ab} = \frac{h \mathbf{u}_{ab} \cdot \mathbf{r}_{ab}}{(r_{ab}^2 + \eta^2)}$$

$$\overline{c_{ab}} = 0.5(c_a + c_b)$$

$$\eta^2 = 0.01h^2$$

In the artificial viscosity expression, α is a coefficient that needs to be tuned in order to introduce the proper dissipation.

3.3.2 Laminar viscosity

When a fluid is flowing through a channel such as a pipe or between two flat plates, either of two types of flow may occur depending on the velocity and viscosity of

the fluid: laminar flow or turbulent flow [39]. Laminar flow tends to occur at lower velocities.

Laminar viscous stresses in the momentum equation can be expressed as:

$$\left(\frac{\mu}{\rho} \nabla^2 u\right)_i = \sum_j \frac{m_j (\mu_i + \mu_j) r_{ij} \cdot \nabla_i W_{ij}}{\rho_i \rho_j (r_{ij}^2 + 0.01h^2)} u_{ij} \quad \text{Eq. 3-11}$$

Where u is the dynamic viscosity coefficient. The $0.01h^2$ term in the denominator is to prevent the denominator equal to 0.

Use average density $\bar{\rho}_{ij} = (\rho_i + \rho_j) / 2$ to replace ρ_i and ρ_j , **Eq. 3-11** could be written as:

$$\left(\frac{\mu}{\rho} \nabla^2 u\right)_i = \sum_j \frac{4m_j (\mu_i + \mu_j) r_{ij} \cdot \nabla_i W_{ij}}{\bar{\rho}_{ij} (r_{ij}^2 + 0.01h^2)} u_{ij} \quad \text{Eq. 3-12}$$

3.3.3 General viscosity

The general form of N-S equation:

$$\frac{du}{dt} = g - \frac{1}{\rho} \nabla P + \frac{1}{\rho} \nabla \cdot \tau \quad \text{Eq. 3-13}$$

τ is the viscous stress tensor, which is proportional to the strain rate tensor ε :

$$\begin{aligned} \tau_{ij} &= \mu \varepsilon_{ij} \\ \varepsilon_{ij} &= \frac{\partial u_i}{\partial x_j} + \frac{\partial u_j}{\partial x_i} - \frac{2}{3} (\nabla \cdot \vec{u}) \delta_{ij} \end{aligned} \quad \text{Eq. 3-14}$$

Where i and j represent coordinates, 1, 2, 3 in the three-dimensional space, corresponding to coordinates x, y, z ; δ_{ij} is the Dirac function.

3.4 Artificial compressibility

The SPH method is used to deal with compressible flow problems. Pressures are calculated by equations of state according to changes in density and internal energy. For incompressible fluid, a slight change in density causes a large change in the pressure gradient, and the pressure is too sensitive to changes in density, which makes the calculation process very unstable and the required calculation time step is too small [42].

The state of equation:

$$p = B \left[\left(\frac{\rho}{\rho_0} \right)^\gamma - 1 \right] \quad \text{Eq. 3-15}$$

B is a parameter that depends on the specific problem:

$$B = c^2 \rho_0 / \gamma \quad \text{Eq. 3-16}$$

ρ_0 is the reference density, c is the sound velocity, γ is the constant, normally equal to 7. The following state equations are usually used. Morris first proposed in the paper:

$$p(\rho) = c^2 \rho \quad \text{Eq. 3-17}$$

Although the two forms of the equation are quite different, they are intrinsically related:

$$\begin{aligned} B \left[\left(\frac{\rho}{\rho_0} \right)^\gamma - 1 \right] &= \frac{c^2 \rho_0}{\gamma} \left[\left(1 + \frac{\rho - \rho_0}{\rho_0} \right)^\gamma - 1 \right] \\ &= \frac{c^2 \rho_0}{\gamma} \left\{ 1 + \gamma \left(\frac{\rho - \rho_0}{\rho_0} \right) + O \left[\left(\frac{\rho - \rho_0}{\rho_0} \right)^2 \right] - 1 \right\} \\ &= c^2 (\rho - \rho_0) + O \left[\left(\frac{\rho - \rho_0}{\rho_0} \right)^2 \right] \end{aligned} \quad \text{Eq. 3-18}$$

As the density gradient changes are very small, so $(\rho-\rho_0)/\rho_0$ can be ignored. The speed of sound is a factor that must be carefully considered. To use an artificial compressed fluid to approximate a real fluid, the speed of sound must be much lower than the actual value. Therefore, the requirements for the speed of sound are: The speed of sound must be large enough that the characteristics of the artificial compressible fluid are sufficiently close to the real fluid; on the other hand, the speed of sound must be small enough to allow the increment of time step within the allowable range. Such adjustment however, restricts the sound speed to be at least ten times faster than the maximum fluid velocity, keeping density variations to within less than 1% [43], and therefore not introducing major deviations from an incompressible approach:

$$c \geq 10 \max(|u|, \sqrt{2gh}) \quad \text{Eq. 3-19}$$

3.5 Results and Discussion

The three-dimensional model of the anesthetic injection was developed according to the procedures detailed in the Introduction. In order to compare the results, this section will discuss the results from the SPH Method and the SEM.

3.5.1 Results for the SEM

As it is mentioned before, the simulation of the solution flowing from the syringe into human skin is divided into two parts.

3.5.1.1 Solution for Simulation of Micro-Needle

In the first part, the length of the needle is set at 1 mm, the radii are set as 50 μm at the bottom, and 25 μm at the sharp (for rectangular cross-section, the widths of bottom and sharp are set as 50 μm and 25 μm). We set the flow as the pressure driven flow. As a

result, the initial velocity at the inlet is set at 0.0, the pressure of the inlet is set at 10.0 kPa, and the outlet is imposed with the Neumann boundary condition.

Figure 3-1 shows the models of the needles with circular and rectangular cross sections. By comparing the results from both of these two models and mapping their data as the initial conditions to our second part of the simulation, numerical solution of the Darcy-Brinkman equations, the results are almost the same. In this section, we take the data of the pressure and velocity from the circular cross-section.

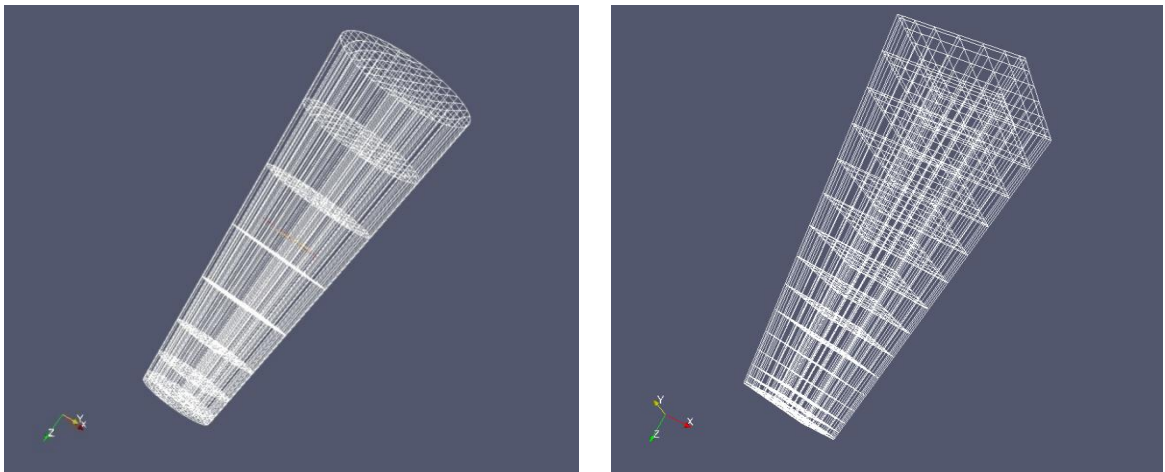


Figure 3-1: the models of needles with circular and rectangular cross sections [85].

After the results are converged, **Figure 3-2** shows the velocity contour on xz-cross section, with the initial pressure of 10 kPa, the normalized velocity comes with a maximum value of 35.9 at the outlet.

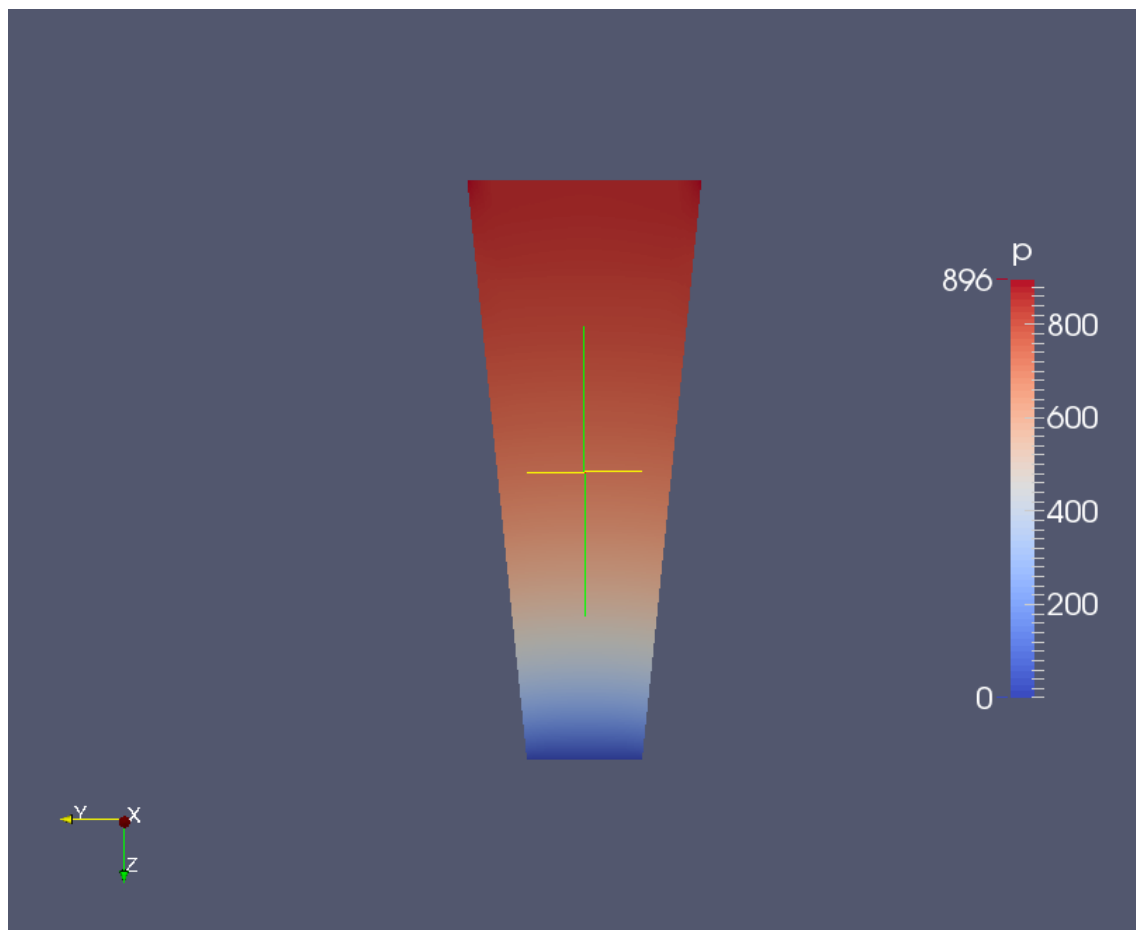


Figure 3-2: the pressure on xz-cross section [85].

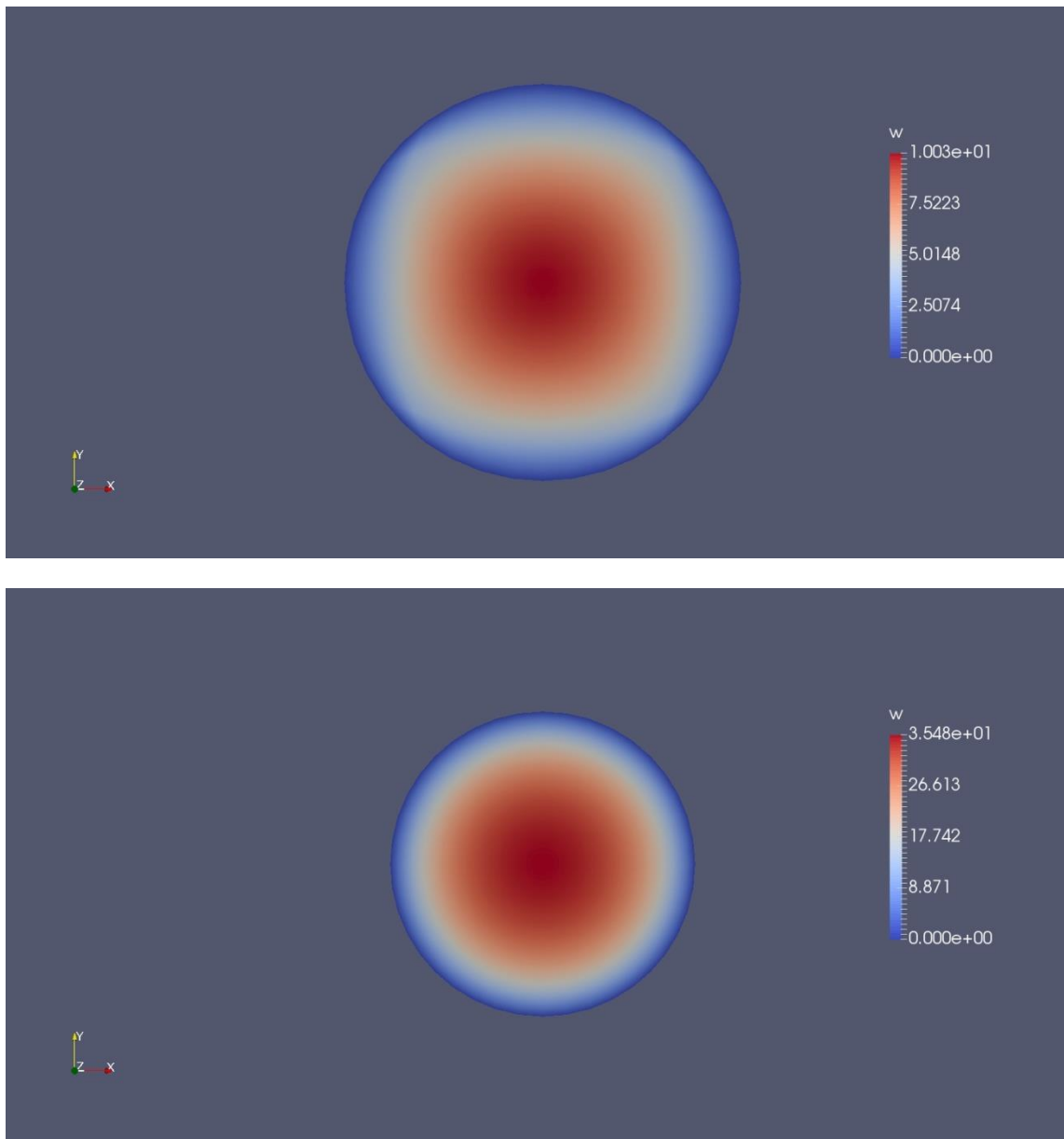


Figure 3-3: the contours of velocity on z-direction at the inlet (up) and outlet (down) [85].

Figure 3-3 shows the normalized velocity of z-direction at the inlet and the outlet. Due to the slip boundary conditions, the velocity near the wall is much smaller than at the middle area. **Figures 3-3** to **3-4** come from the simulation of the model with the 3rd order.

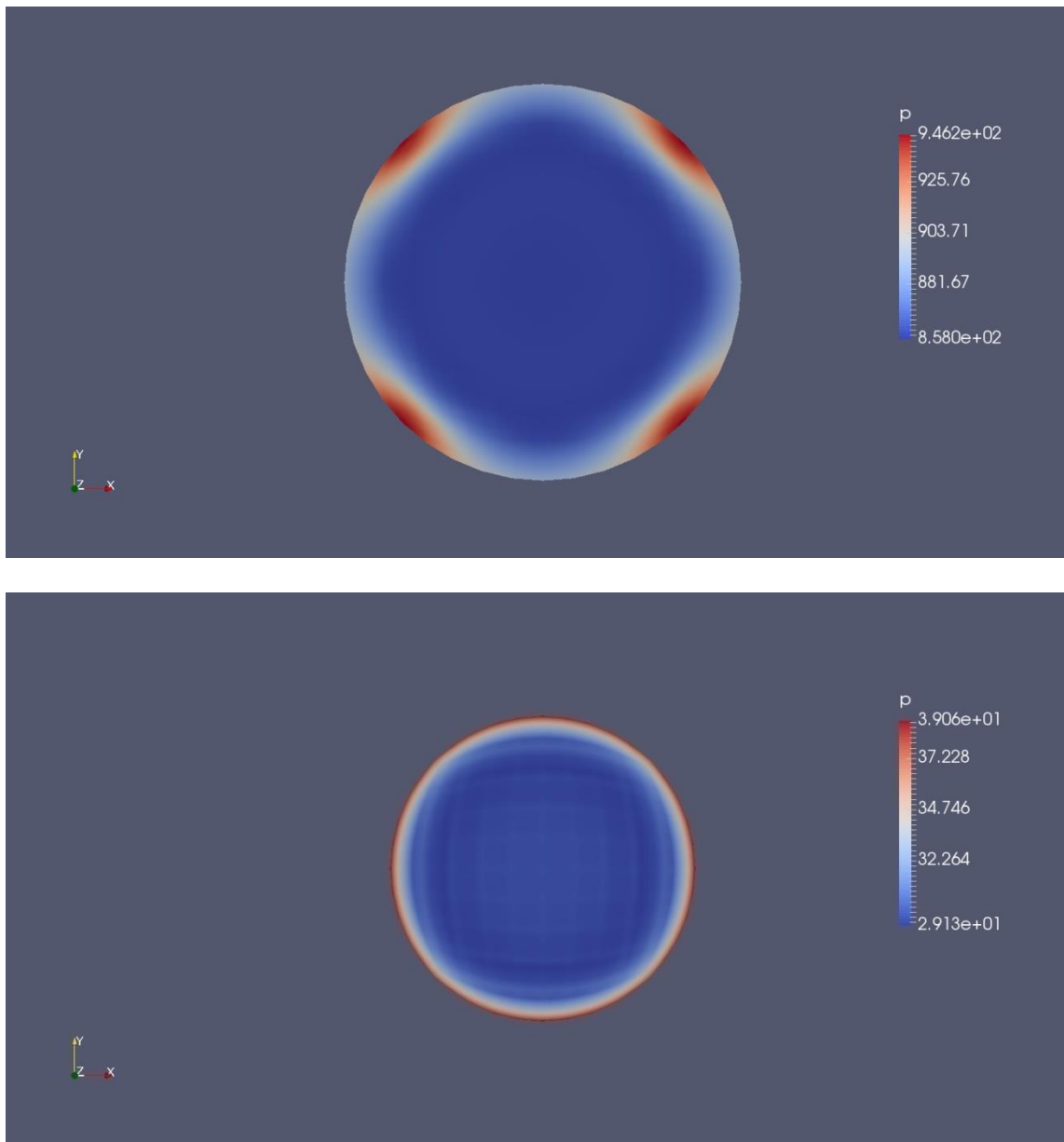


Figure 3-4: the contours of pressure at the inlet (up) and outlet (down) [85].

Figure 3-3 shows the contours of pressure at the inlet and outlet of the needle. As mentioned before, the data from the outlet of the needle will project to become the input boundary and initial conditions of the next model. The polynomial order of the basis functions needs to be the same. For example, the 3rd order scheme of the needle can only

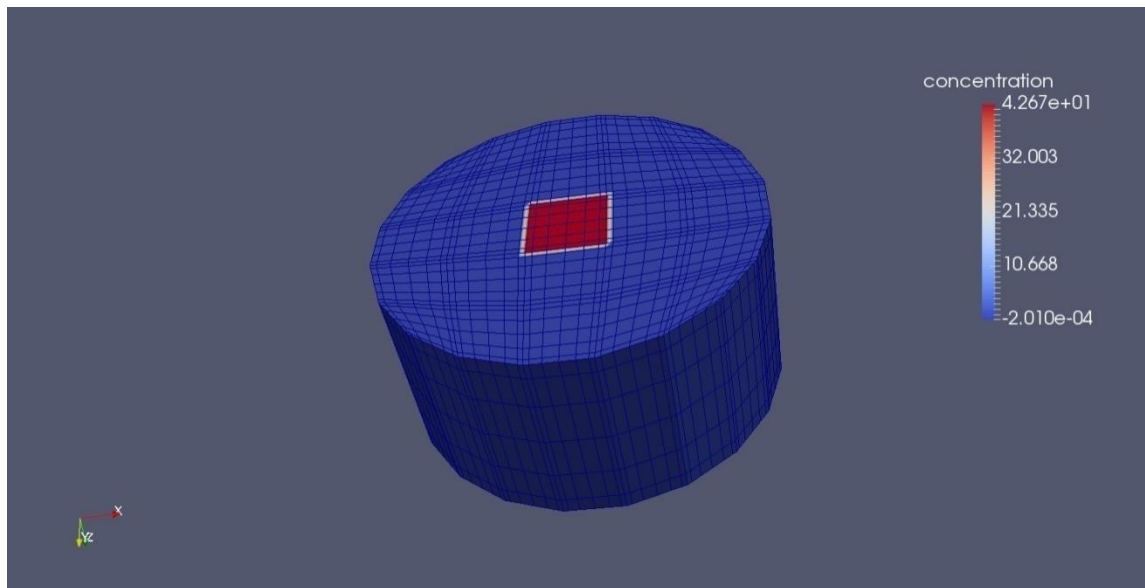
match the 3rd order model of human skin. When the 5th order simulation for human skin is analyzed, the order for the needle will also be increased to the 5th order.

3.5.1.2 *Solution for Simulation of Human Skin*

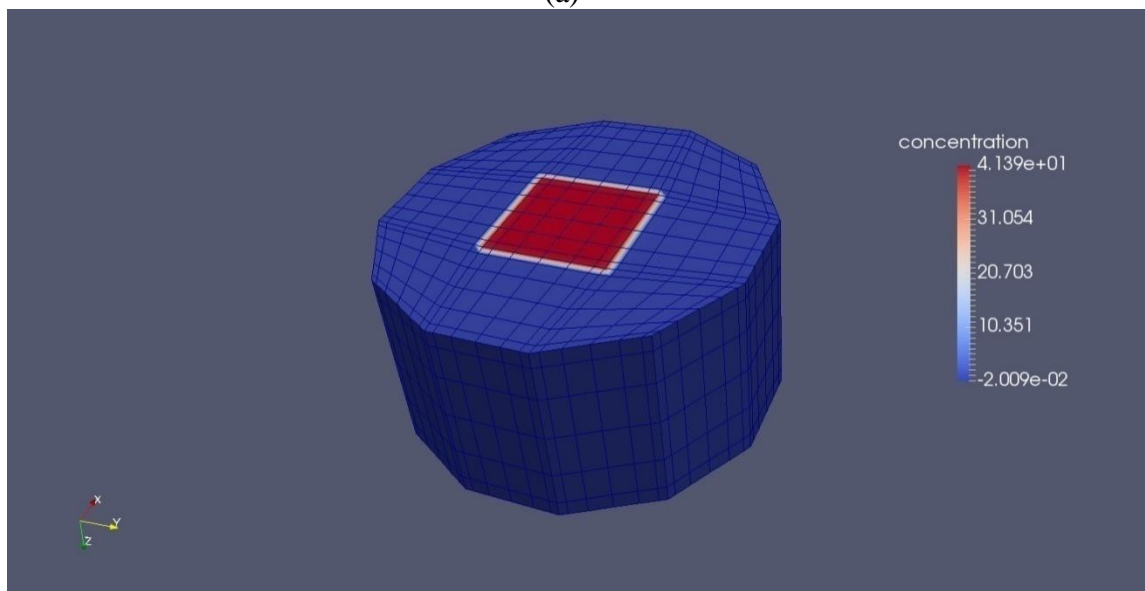
In this section, human skin is simplified as a cylinder. The top of the cylinder is treated as the cross section of the skin where the needle pierces. The bottom represents the interface of the dermis and the fat layer. In this case, we do not need to simulate all these areas from the surface of the skin to the bottom of the fat layer. It can largely reduce the number of elements in our models, which in turn will save time on running the code. There are two different schemes for simulation. The first one is single needle with the same number of elements and different order of the basis functions and initial conditions. The other one is multiple needles with a different number of elements, and the same order of the basis functions and initial conditions.

3.5.1.2.1 Single Needle

Figure 3-5(a) shows the contour map of the initial concentration for the single needle case. At time = 0, the initial concentration at the surface of the skin is set at 42.67 mol/m^3 according to **Table 3-1**. By doing some tests on different models, we find that by changing the ratio of the needle's input area to the area of the x-y cross section of the model, the result's range (maximum and minimum values of models) will also be seriously changed (see **Figure 3-7**). The result will become convergent when the ratio decreases to about 0.05. However, if we built models with a ratio of 0.05 or less, it will largely increase the number of elements or the order of the basis functions, which will take a much longer time to run our codes.

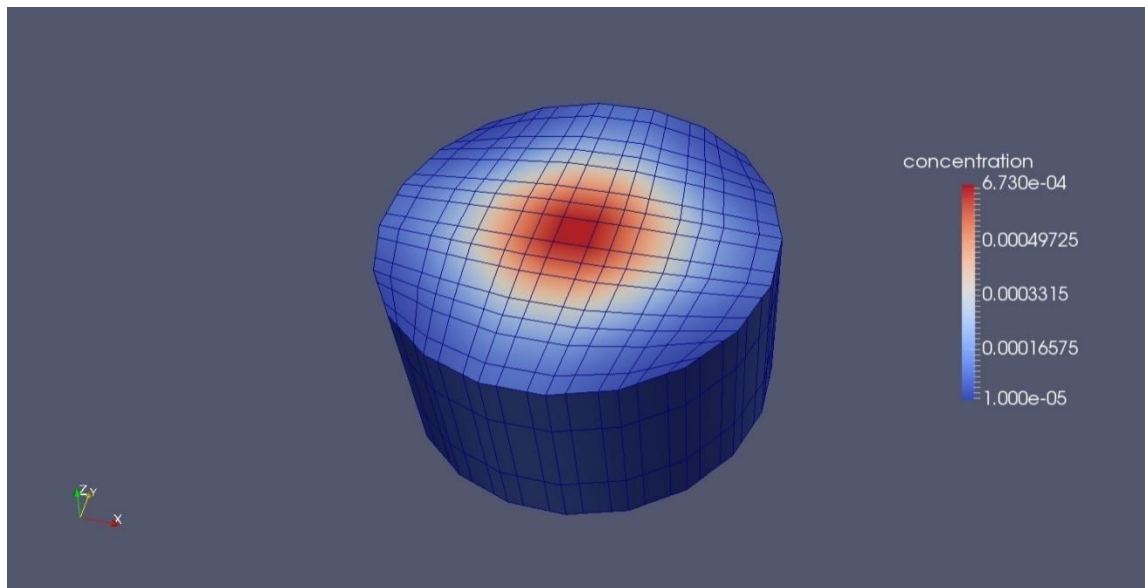


(a)

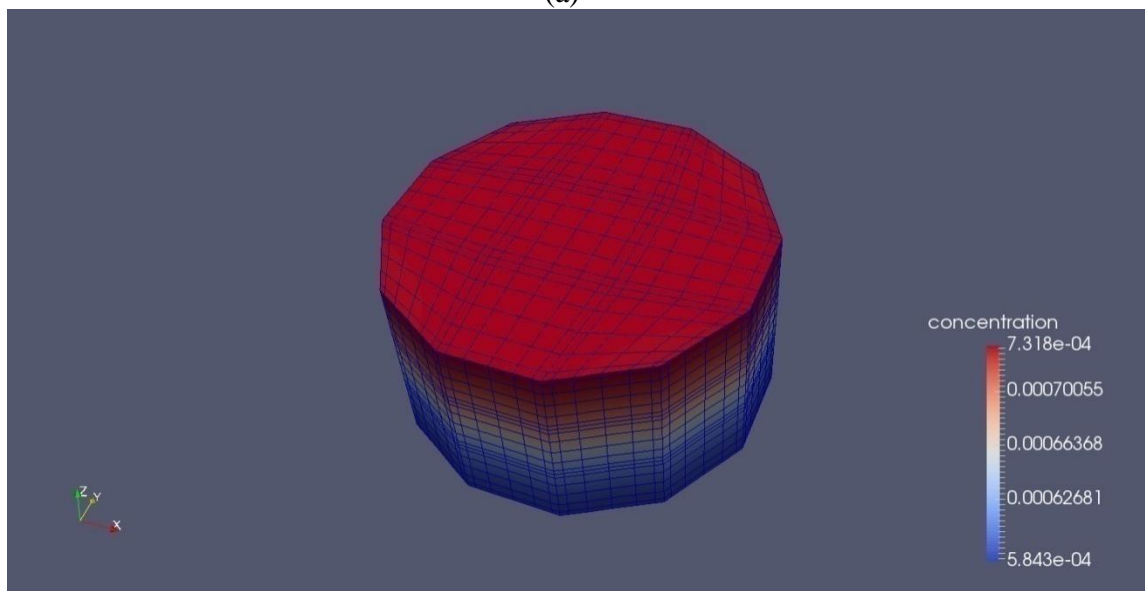


(b)

Figure 3-5: the initial contours of concentration with a different ratio of a needle's input area to the area of x-y cross section of model [85]. (a): The model of human skin with a single needle at a ratio of 0.05. (b): The model of human skin with a single needle at a ratio of 0.1.



(a)



(b)

Figure 3-6: contour maps for the single-needle model at $t = 60$ sections with different ratios of needle input area to the area of the x-y cross section [85]. (a): the concentration of 4th order bases and 75 elements with a ratio of 0.05. (b): the concentration of 6th order bases and 45 elements with a ratio of 0.1.

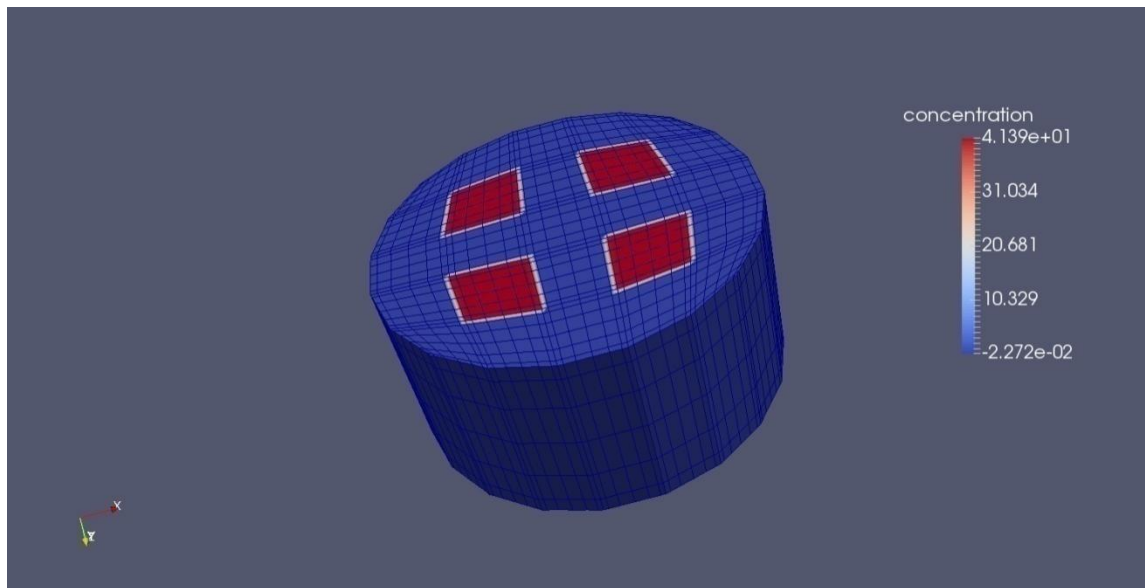
In **Figures 3-6 (a)** and **(b)**, the maximum and minimum concentrations of the first cases are 6.370×10^{-4} and $1.000 \times 10^{-5} \text{ mol/m}^3$. On the other hand, for the second case,

the maximum and minimum concentrations are $7.318 \times 10^{-4} \text{ mol/m}^3$ and $5.843 \times 10^{-4} \text{ mol/m}^3$, respectively. It seems that for this type of model, with every parameter due to references, the result for the concentration is much less than its necessary value $4.267 \times 10^{-3} \text{ mol/m}^3$. Since the critical area for this model is the concentration at the interface between the dermis and the fat layers, we decide that instead of reducing the ratio, we will focus on the concentration of the critical area directly under the needle. To improve the result for our model, there are two possible ways. The first one is increasing the initial concentration, and the second way is keeping the sizes of the model but using multiple needles. Since even if the concentration requirement can be achieved by the first approach, the practical application needs not only concentration, but also enough dose. We decide to develop a model with four micro needles on top. Simultaneously, in this model, the critical area is the cross section of the dermis-fat layer interface under and between the needles. We try to find the concentration of the drug in this area, which is affected by multiple needles. The following paragraph will discuss the results from the models with four needles.

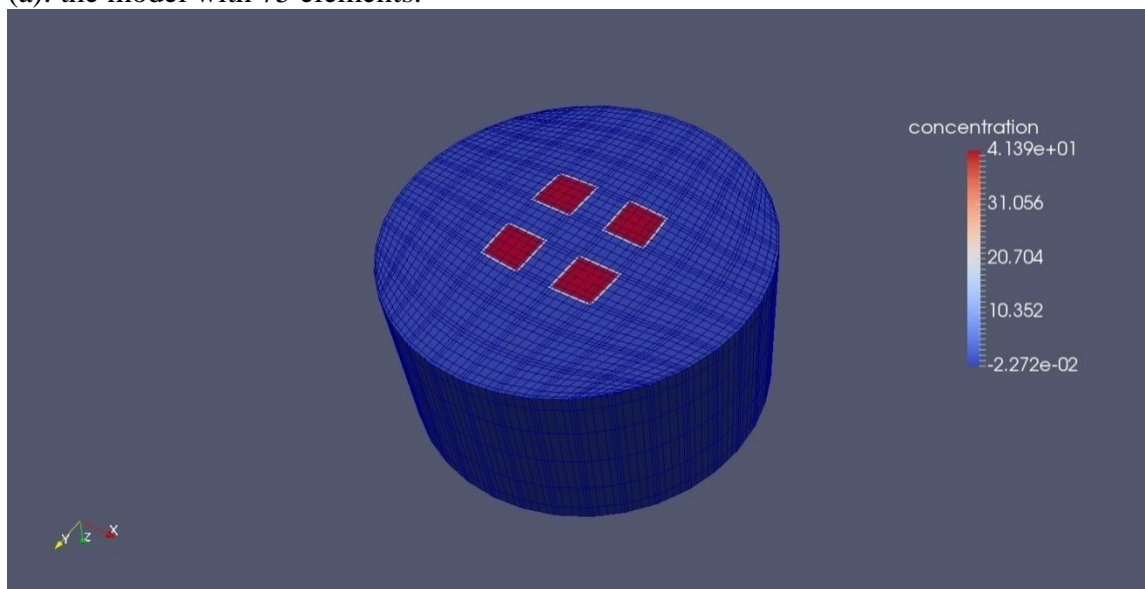
3.5.1.2.2 Multiple Needles

Based on the Single-Needle model, we develop another model with 4 needles.

Figure 3-7 and **Figure 3-8** show the modified models of the 6th order bases with 75 and 243 elements. By comparing the results from these two models, the maximum and minimum concentration have the differences of 4.32% and 4.12%; due to this fact, it seems unnecessary to increase the number of elements or the order of the basis functions anymore.



(a): the model with 75 elements.

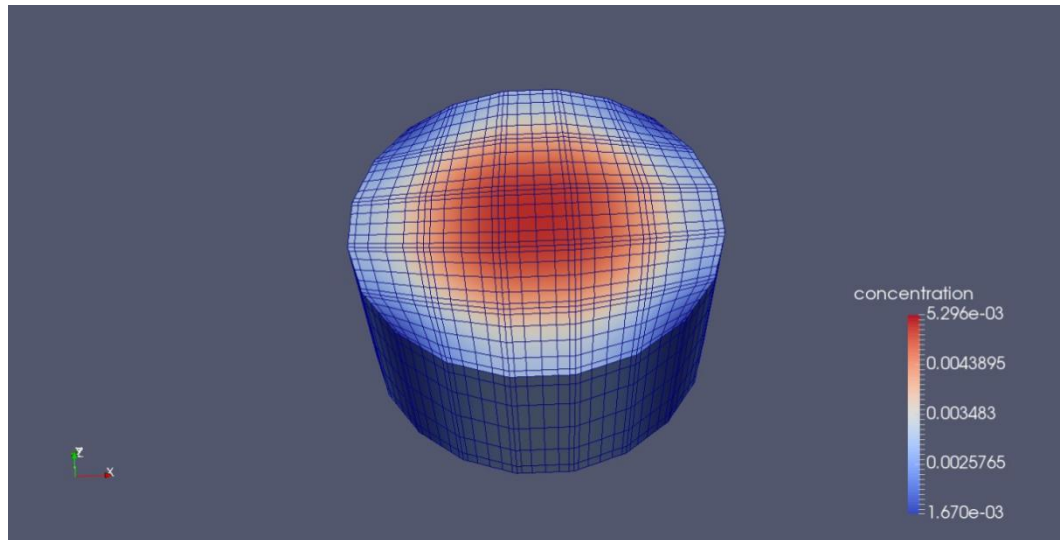


(b): the model with 243 elements.

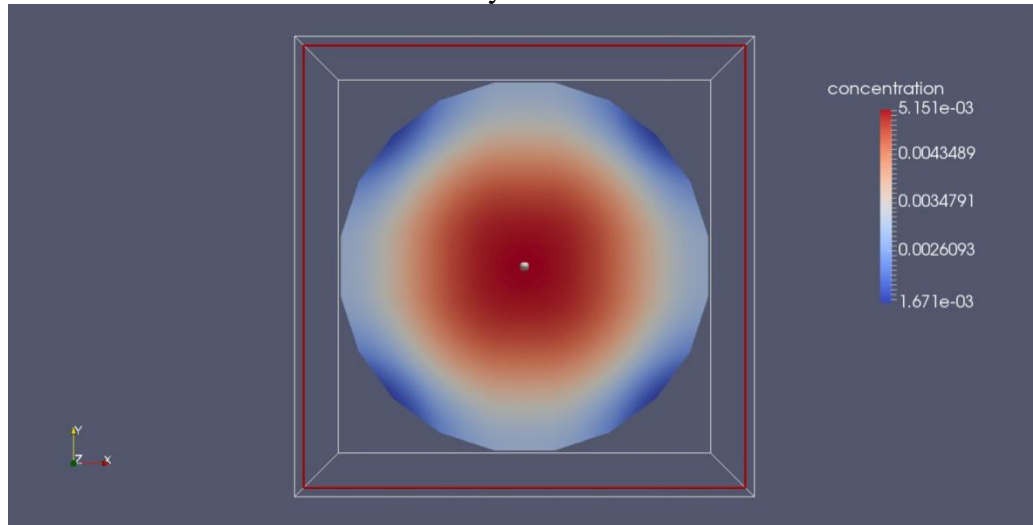
Figure 3-7: the initial models of human skin with 4 needles [85].

After the result converges, the contour maps of concentration with the 6th order accuracy are shown in **Figure 3-7**. In **Figure 3-7(a)**, the minimum value of concentration is $1.670 \times 10^{-3} \text{ mol/m}^3$, which is lower than the minimum necessary value, while the maximum concentration is $5.296 \times 10^{-3} \text{ mol/m}^3$, which is beyond the required value.

Moreover, from **Figure 3-7(b)**, the highest concentration located at the middle of the critical layer is also the middle of the 4 needles. The value is $5.151 \times 10^{-3} \text{ mol/m}^3$, which is 20.71% larger than the required concentration.



(a) concentration with 6th order accuracy.



(b) concentration at interface of the dermis and the fat layer.

Figure 3-8: contour maps for 4-needle model at $t = 60$ sections [85].

3.5.2 SPH simulation results

In this section, we simulate a two-dimensional SPH model for the micro needle and compare the results with other modeling data. The total number of drug particles is 1200. Due to the effect of body fluids, a 0.0005 N downward force is added on the drug particles. The drug particles and porous media particles have the same value of the mass. Blue particles are used to represent drug molecules, while white particles as a random distribution of the fixed point are used to simulate the porous medium. After the micro needle pierces the surface of the skin, particles of the internal drug will go through the porous medium and then get into the capillaries and transport to all parts of the body via blood flow. **Figure 3-9(a)** indicates the initial conditions for the micro needle simulation. In **Figure 3-9(b)** and **Figure 3-9(c)**, drug particles dispersed in most of the upper part. With time increasing **Figure 3-9(d)**, drug particles dispersed everywhere in the porous medium.

Figure 3-10 is the number of particles with a depth beyond 2000 μm , which equals to the concentration change in the lower part of the middle. It is similar compared with [71] which come from the spectral element method. SPH model has a 0.0005 N downward force which signifies this model is closer to the actual situation. There are still some reasons that cause system errors. Firstly, the error is caused by using fixed random distribution particles to build the dermal layer of the porous medium structure. Secondly, due to the random distribution of the particles, the results have small differences every time. Thirdly, for the continuous modeling, the permeability of the skin can be defined exactly by a parameter; however, for the discrete modeling, it is hard to control this parameter with accurate measurement.

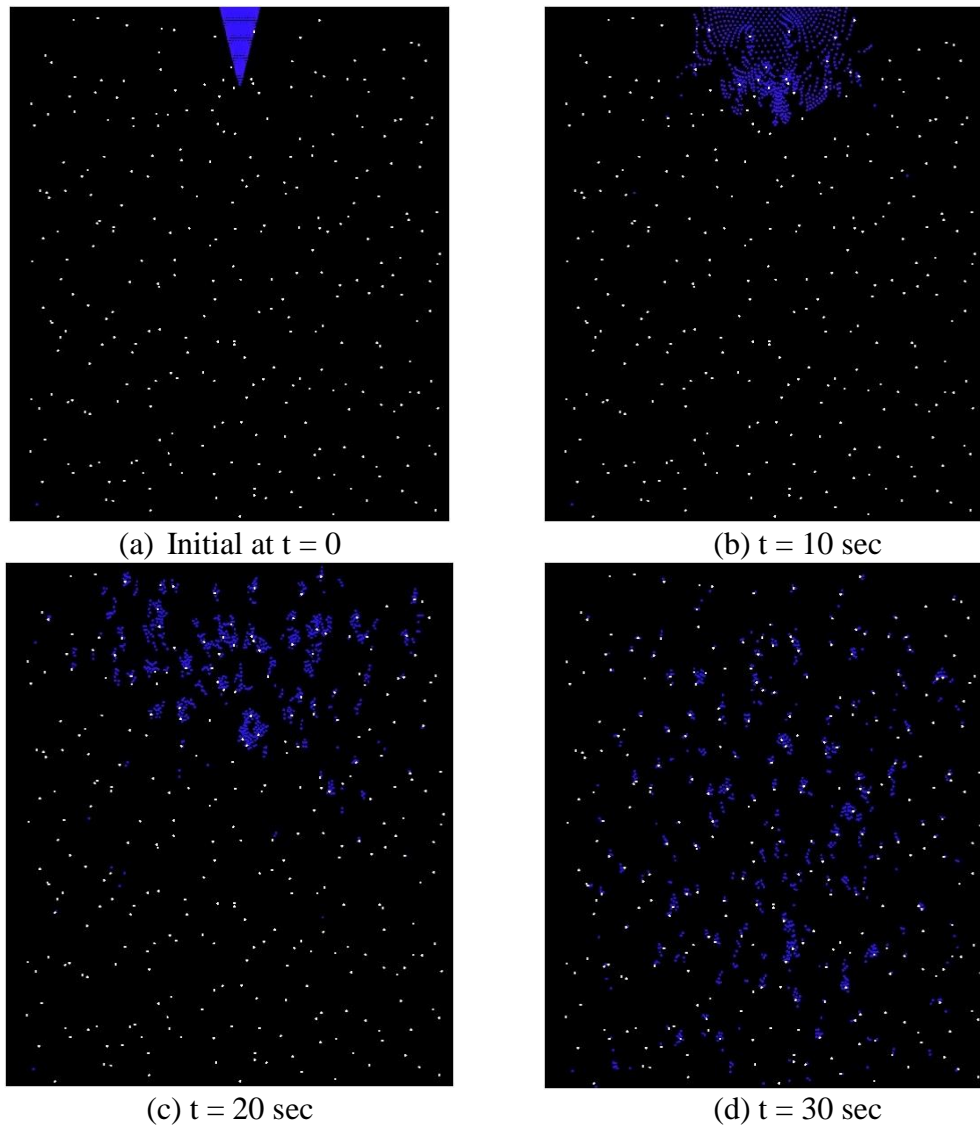


Figure 3-9: the motion process of drug molecules.

In this paper, one continuous (mesh-based) and one discrete mesh-free simulations using totally different formulations and methods were utilized to help understand some details of drug delivery in the microneedle. The diffusion speed of drug particles was found to be anisotropic from both simulations, especially in the vertical direction, although isotropic porosity was used in both simulations. This is mainly due to the initial momentum - pushing of the microneedle. At the center of the microneedle, the

concentration is higher than the surrounding areas from both simulations even under the same conditions. According to the initial concentration of 42.67 mol/m^3 and the interior volume of the microneedle $2.51 \times 10^{-11} \text{ m}^3$, the dosage of drug in the microneedle is $1.072 \times 10^{-9} \text{ mol}$. That means there are 6.46×10^{14} drug molecules in total.

A circular cone built with 6,460 points was used to represent the microneedle. There are 1,200 SPH points in the computational domain consisting of a cylinder with 4 mm in height and 2.5 mm in radius; therefore, the volume of the microneedle in this simulation is $1.963 \times 10^{-8} \text{ m}^3$. From the plot of three groups in the simulation we could achieve that in the mesh-free simulation that almost 50% of the medicine particles reached the deeper layer after 30 seconds. The average concentration in the deeper layer is about 0.0054 mol/m^3 . This result means that the dosage in the deeper layer is beyond 0.004267 mol/m^3 , the minimum concentration in Table 1. The average concentration beyond 2mm in depth means drug particles already touch the blood, and the blood will carry drug particles and deliver to any part of the body. SPH results indicate the same conclusion with SEM and the reference work in [4] regarding the concentration at the interface of the dermis and fat layers.

Using almost the same parameters as in SEM and SPH 2D simulations, but some differences in the results exist. The reasons include the following points: The SPH simulation of one microneedle indicates that almost half of the drug particles reached the capillary layer after 30 seconds. On the other hand, results from SEM show that drug particles almost spread out to most parts of the domain within 60 seconds. These differences are mainly attributed to different formulations and methods used. First, SEM used fully 3D computational model while SPH used a 2D. In order to make the result

more persuasive I built a 3D SPH simulation. Second, SEM is continuous but SPH is discrete in the model's description. We use a different way to operate the discrete formations. Third, spatial resolutions are different. SEM uses finite elements and high order polynomial expansions for increased resolution, whereas SPH uses many randomly distributed discrete particles. Consider the limit of computation ability; use one particle to represent the molecule cluster. This is also an important reason in term of different results.

Figure 3-10 indicates numerical result of 2D microneedle simulation. Because fixed particles are randomly distributed in the computational domain to represent porous media, it will generate fixed particles a little differently every time you run codes. There is a slight difference in the results of each generation. In order to avoid this difference in results, we ran it several times and plot results on one figure. There are three trials in **Figure 3-10** and each trial represent one result. This figure demonstrates randomly distributed particles have no big effect on the results.

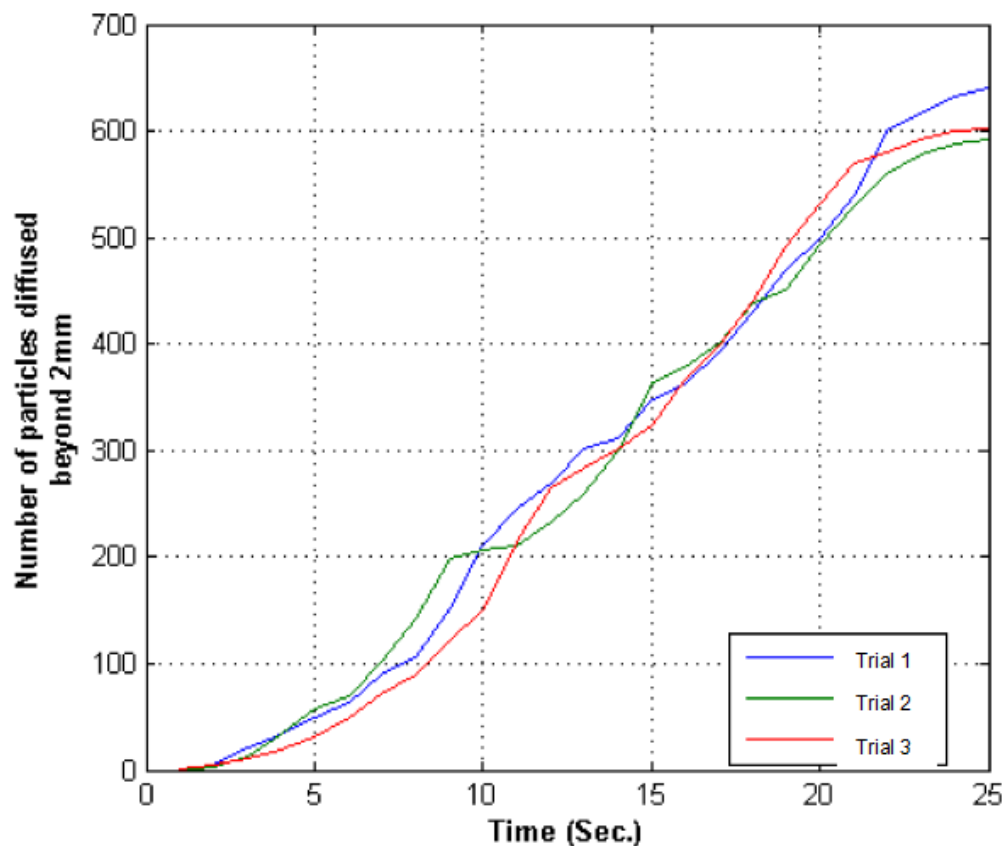


Figure 3-10: the number of particles that has a depth beyond 2000 μm in the 2D model.

3.6 3D microneedle simulation by SPH

In order to further demonstrate that the microneedles make a significant sense to clinical medicine and fixed errors in 2D SPH simulation, we carried out the 3D SPH simulation which uses the same parameters in Table 1. The total number of molecules is about 12,000, the drug molecules are about 8000, and the rest is randomly distributed porous medium points. The height and radius of a cylinder computational domain are 4 mm and 2.5 mm; therefore, the volume is $1.963 \times 10^{-8} \text{ m}^3$ same with 2D simulation.

Figure 3-11 to **Figure 3-14** indicate process of drug particles movement.

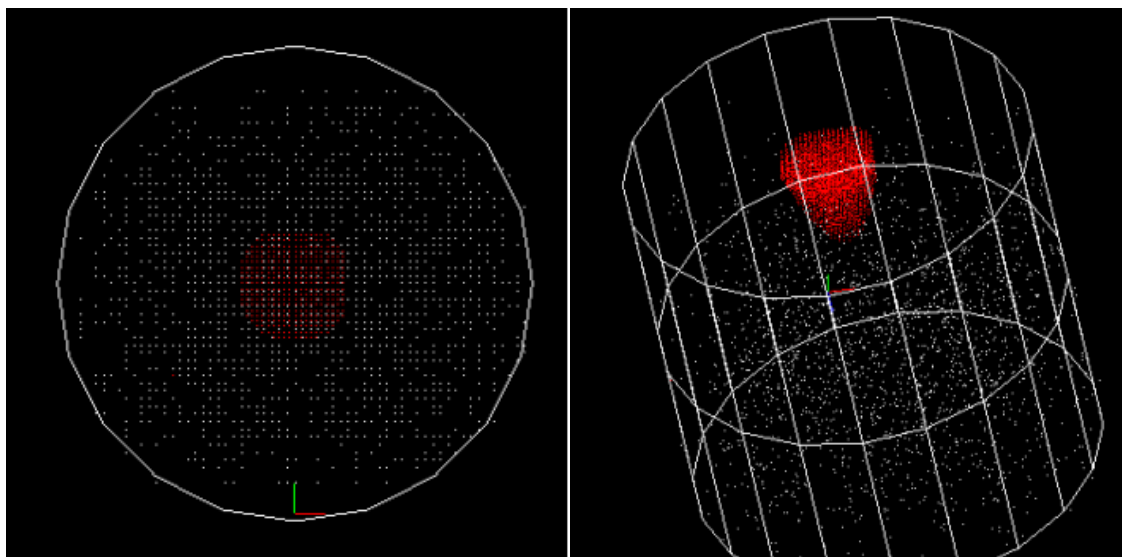


Figure 3-11: initial condition of 3D microneedle simulation.

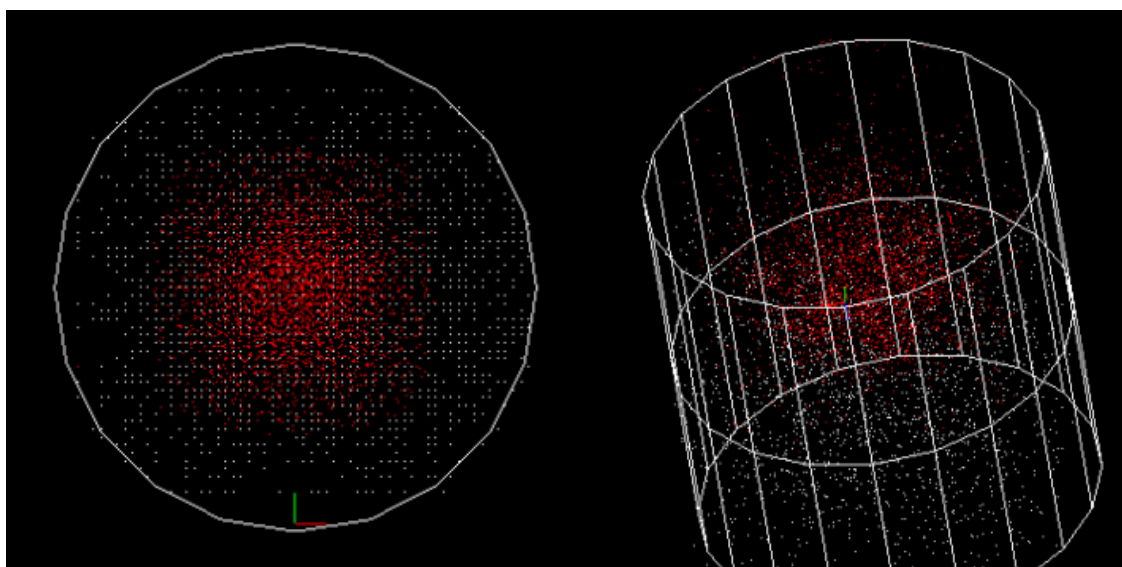


Figure 3-12: 20 seconds of 3D microneedle simulation.

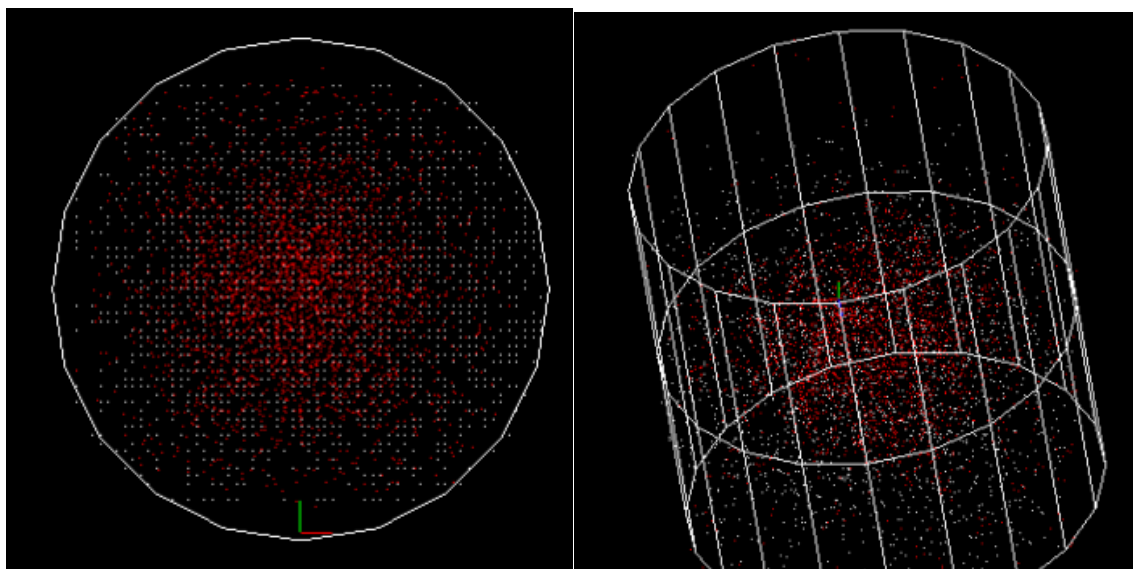


Figure 3-13: 40 seconds of 3-D microneedle simulation.

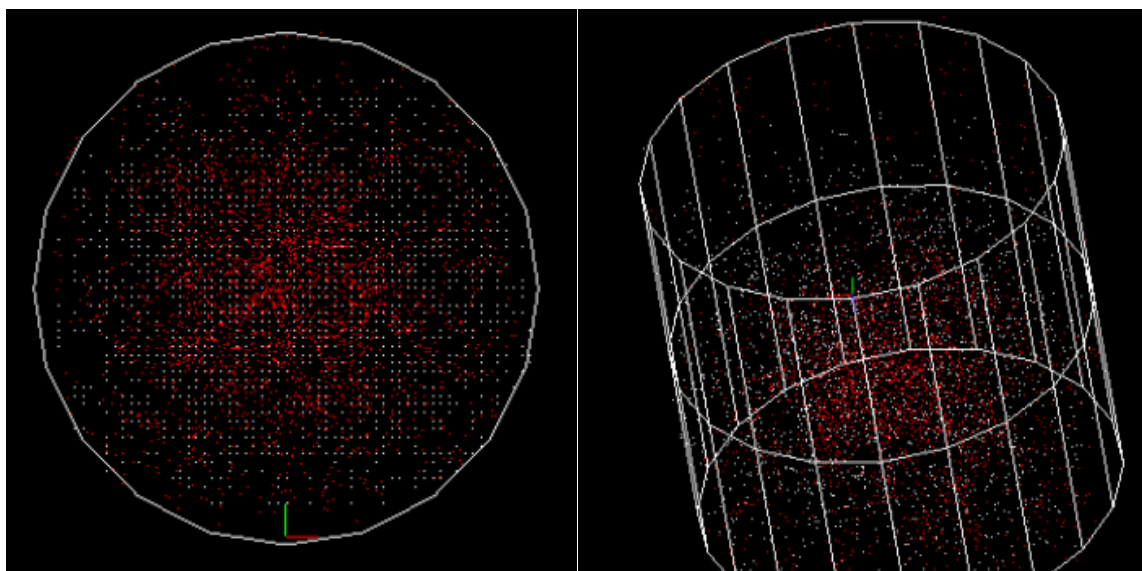


Figure 3-14: 60 seconds of 3D microneedle simulation.

The figures demonstrate the entire process of the drug particles spreading from the initial setting to the drug molecules that filled out the computational domain. At the beginning, the drug molecules stay in the microneedles, and gradually spread towards the

cross-section of dermis-fat layer interface. The drug molecules gradually filled the entire model in 60 s. Results of SEM and SPH two methods are highly similar after comparing the two processes of diffusion, 60 s later, around 4,700 particles pass through the cross-section of dermis-fat layer interface. About 6,300 particles pass through the cross-section of dermis-fat layer interface after 120 s Fig. 3-13. This proves the microneedles can replace the existing injection of the syringe. In this simulation, the critical area is the cross-section of dermis-fat layer interface under and between needles which determines the drug delivery dosage. **Figure 3-15** indicates 60 secs cross-section of a 3-D microneedle simulation. **Figure 3-15** shows the number of particles passes the fat layer.

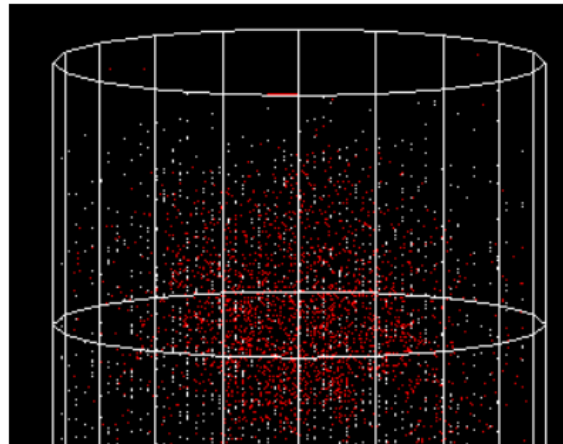


Figure 3-16: 60 secs cross-section of a 3-D microneedle simulation.

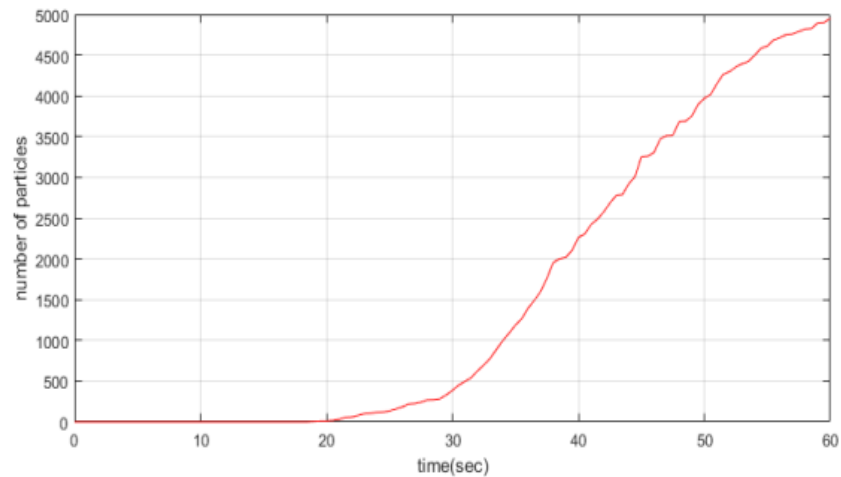


Figure 3-17: the number of particles passes the fat layer.

3.7 Conclusion

Compared with traditional injection syringes, micro needles are painless, easy to operate, and a possible alternative to avoid the spreading of blood borne infections. To search online, there are already micro needle products. Different kinds and shapes of needles [81, 82] and their clinical trials [83] are discussed in detail based on experimental tests and investigations. In this paper, numerical methods with high order accuracy are conducted to show a good agreement with these reference experimental data.

This paper developed virtual models to simulate the flux of Lidocaine from the needle into human skin. The drug in the micro needle is simulated as a pressure driven Navier-Stokes equations with a slip boundary condition. Also, the drug spreading in human skin is treated as the Darcy-Brinkman equations. Since there are not too many numerical results to compare with, we do convergent tests for both h-refinement, p-

refinement (SEM), and discrete method (SPH). The result shows the micro needle patch that with the current parameters, the drug can fully transfer to the required concentration.

At the same time, our two-dimensional three-dimensional model of the SPH method also shows the match of concentration at the interface of the dermis and the fat layers with SEM and reference. The differences happen due to the initial setting of the model. Since there is a very small initial and boundary condition of pressure, all the drag particles are driven towards the bottom of the model. To minimize the error occurring by this setting, we just account for the number of particles moving through the critical section during 0 to 30 seconds for two-dimensional simulation and 0 to 60 seconds for three-dimensional simulation. The results show that at 50 seconds, the number of drag particles below the interface satisfies the requiremen

CHAPTER 4

CONSTRUCTING A THROMBUS MODEL WITH SPH

The cardiovascular system is the kernel system of the physiological system. Due to people's daily dietary imbalances, smoking, and lack of exercise, the incidence of cardiovascular diseases is increasing. Thrombosis is the most direct factor cause of sudden cardiovascular and cerebrovascular diseases. This article discussed the methods of modeling vascular simulation and using SPH method simulate 25% stenosis blood vessel model and 75% stenosis blood vessel model. The numerical results of the simulation are important for understanding the details of the effect of thrombus on blood circulation. Modeling and simulating the blood vessel provides a guide for studying thrombus disease and an assistant tool for designing the medical equipment.

Thrombosis may occur anywhere in the body where there are arteries. At the same time, this is also the main cause of the lack of oxygen in the heart, brain and other organs and accelerate the aging process. The World Health Organization (WHO) calls for prevention and cure of thrombosis to be health and longevity. Scientific research shows that health erythrocyte has a negative charge outside the membrane. Erythrocytes always maintain a distance from each other due to the mutually repulsive electric fields between the same type charges. Food habits, tobacco and alcohol will cause the charges on the erythrocyte membrane disappeared. Erythrocytes lose their mutual repulsive electric field, resulting in a large number of cell aggregation. It will also reduce the effective

surface area of the erythrocyte membrane and the oxygen-carrying capacity. Eventually, blood clots form in the blood vessels.

Thrombosis can be divided into red, white and fibrin thrombus regarding traits. The red thrombus mainly consists of the erythrocyte and fibrin. The white thrombus is mainly composed of platelets and fibrin. The platelets adhere to and agglutinate on the damaged blood vessel wall, and at the same time, fibrinogen is converted into fibrin to form a thrombus. Fibrin thrombosis is caused by hyperthyroidism in the systemic coagulation system. When the blood vessels are blocked by embolism, the blood flow is interrupted; embolic diseases are formed. After thrombosis generated, the influence of thrombus on blood flow is difficult to study by experiment and observation.

In this paper, in modeling and simulating the blood flow, vessel used the SPH method. SPH is an effective numerical method that can be used to solve a variety of difficult problems in computational mechanics. It is a fully Lagrangian meshless method ideal for solving deformation problems such as complex free surface fluid flows, but SPH is mainly used to simulate free-surface such as water waves, less application in physiological fluids. Due to these advantages, it is suitable to simulate a blood vessel model by SPH method achieve the ideal result.

4.1 Introduction

In this simulation, there are several advantages compared to the previous models such as:

1. Erythrocyte could deform when a collision occurs. It is well known that erythrocyte could change their shape to pass through narrow capillaries and deliver oxygen into tissues and cells. In this model,

deformation will occur when the boundary or erythrocyte receive external forces or collisions.

2. In this model, the periodic of external force is 0.8 s, close to the frequency of a heartbeat and vasoconstriction.
3. In order to optimize the simulation effect, a shifting algorithm was added to the model to avoid the phenomenon of the local density being too low in the calculation process.
4. In some existing vessel simulations, a constant velocity is applied to the elements directly as a drive force. These models are too simplified for real situations. In our model, we put drive force on the inlet surface of the vessel model and erythrocytes flow with the bloodstream in the vessel.

There are also some advanced techniques applied to this thrombus simulation such as Linked-list search algorithm and symplectic algorithm. So the results of this simulation are very convincing.

For this thrombus simulation, B-spline function is chosen for the kernel function. The blood flow appears as a laminar flow at low velocity in the vessel, and most particles move in a straight line along a direction parallel to the boundary of vessel. The flow rate of the blood is greatest at the center of the vessel and smallest near the boundary. Based on the simulation, laminar viscosity is selected as viscosity term in this simulation. There are about 50,000 timesteps in this simulation. Consider the accuracy and stability of the simulation; the symplectic algorithm is a good choice. Because symplectic algorithm

preserves geometric features, such as the energy time-reversal symmetry present in the equations of motion, it improves the resolution of long-term solution behavior.

Dynamics boundary condition is applied to the vessel model to indicate the pressure of boundary particles, and the inlet and outlet use periodic boundary condition to imitate the inflow and outflow of the blood.

The following sections will talk about the selection of time step algorithm, the selection of neighbor particles search algorithm, and some related problems.

4.2 Time step

Numerical integration of the discretized SPH equation requires a suitable time step. The selection of the time step is critical. If the time step is too small it will increase the calculation amount; if the time step is too long, it will lead to distortion or collapse of the calculation. Since the time step is related to the state change of material and directly affects the accuracy and stability of numerical calculation, the time step selected for explicit time integration must satisfy the CFL (Courant-Friedrichs-Levy) condition [55]. CFL condition means the time step must be less than a certain time in CFD; otherwise, the simulation produces incorrect results. In SPH, the CFL condition requires that the time step should be proportional to the minimum value of the distance between particles. Convert CFL to time step proportional to a minimum smooth length in the SPH:

$$\Delta t = \min \left(\frac{h_i}{c} \right) \quad \text{Eq. 4-1}$$

Monaghan gives an expression that considers viscous dissipation and external force, respectively:

$$\Delta t_{cv} = \min \left(\frac{h_i}{c_i + 0.6(\alpha_{\Pi} c_i + \beta_{\Pi} \max(\varphi_{ij}))} \right) \quad \text{Eq. 4-2}$$

$$\Delta t = \min \left(\frac{h_i}{f_i} \right)^{\frac{1}{2}} \quad \text{Eq. 4-3}$$

In the equation, f is the force effect on unit mass. Use the equations above and add two coefficients $\lambda_1 = 0.4$ and $\lambda_2 = 0.25$ [60], the standard time step could be calculated by the following equation:

$$\Delta t = \min(\lambda_1 \Delta t_{cv}, \lambda_2 \Delta t_1) \quad \text{Eq. 4-4}$$

4.2.1 Verlet scheme

The Verlet scheme is based on the common Verlet method. The predictor step calculates the variables according to:

$$\begin{aligned} \frac{dv_a}{dt} &= F_a \\ \frac{d\rho_a}{dt} &= D_a \\ \frac{dr_a}{dt} &= v_a \end{aligned} \quad \text{Eq. 4-5}$$

However, every time step and variables are calculated according to:

$$\begin{aligned} v_a^{n+1} &= v_a^{n-1} + 2\Delta t F_a^n \\ r_a^{n+1} &= r_a^n + \Delta t V_a^n + 0.5\Delta t F_a^n \\ \rho_a^{n+1} &= \rho_a^{n-1} + 2\Delta t D_a^n \end{aligned} \quad \text{Eq. 4-6}$$

This second part is designed to stop divergence of integrated values through time as the equations are no longer coupled.

4.2.2 Symplectic scheme

Symplectic integration algorithms are time reversible in the absence of friction or

viscous effects. They can also preserve geometric features, such as the energy time reversal symmetry present in the equations of motion, leading to an improved resolution of long term solution behavior [65]. The scheme used here is an explicit second-order Symplectic scheme with an accuracy in time of $O(\Delta t^2)$ and involves a predictor and corrector stage. During the predictor stage, the values of acceleration and density are estimated at the middle of the time step according to:

$$\begin{aligned} r_a^{n+\frac{1}{2}} &= r_a^n + \frac{\Delta t}{2} v_a^n \\ \rho_a^{n+\frac{1}{2}} &= \rho_a^n + \frac{\Delta t}{2} D_a^n \end{aligned} \tag{Eq. 4-7}$$

During the corrector stage $dv_a^{n+\frac{1}{2}}/dt$ is used to calculate the corrected velocity, and therefore the position of the particles at the end of the time step according to:

$$\begin{aligned} v_a^{n+1} &= v_a^{n+\frac{1}{2}} + \frac{\Delta t}{2} F_a^{n+\frac{1}{2}} \\ r_a^{n+1} &= r_a^{n+\frac{1}{2}} + \frac{\Delta t}{2} v_a^{n+1} \end{aligned} \tag{Eq. 4-8}$$

and finally, the corrected value of density $d\rho_a^{n+1}/dt = D_a^{n+1}$ is calculated using the updated values of v_a^{n+1} and r_a^{n+1} . In this simulation, I choose the symplectic scheme for the time step algorithm. The symplectic scheme provides a more stable precision for a simulation which have large time steps. The symplectic scheme has two steps, one is the predictor stage which uses position and velocity from the last time step to predict the next half time step's position and also for density of particles. The second step use velocity and position to correct the results.

After these two steps, the result shows high stable property, which is very important for large scale and long simulation time models.

4.3 Nearest neighbor particle search

In SPH method, the kernel function has a support domain which uses the selected particle as the center. The radius of the support domain is equal to kh . Particles in the selected particle's support domain are called nearest neighbor particles. The first operation in every time step is to search the nearest neighbor particles of the selected particle. The process of finding the nearest neighbor particles is often called the nearest neighbor particle search (NNPS). In grid methods, once the grid is well-defined, the position of the grid node will not change. However, in the SPH method, the position of the discretized particle changes at each time step. Therefore, it is necessary to re-determine the neighboring particles in the central particle support domain at each time step.

4.3.1 All-pair search algorithm

All-pair search, also called as direct particle search, is a straightforward NNPS method. Because this process of finding neighboring particles operates on all particles, the degree of complexity of the all-paired search method is $O(N^2)$. In the SPH interpolate operation, the NNPS process is performed in each time step operation. Therefore, the all-pair search method consumes for a long time and is not suitable for calculating a large number of particles.

4.3.2 Linked-list search algorithm

Monaghan discusses the process of using the linked list search to implement the nearest neighbor particle search. When implementing the linked list algorithm, a temporary grid should be laid on the problem domain. The space size of the grid unit should be chosen in accordance with the space of the support domain. The linked list

search method distributes each particle within a grid cell and connects all the particles in each grid through a storage rule. If the average number of particles in each cell is small enough, the complexity of the linked list search method is $O(N)$. The disadvantage of the linked list search method is when the smooth length is a variable, and the grid unit cannot adapt to each particle. However when the smooth length is a constant, the linked list search method is very effective.

In this simulation, I use linked list search algorithm to calculate the nearest neighbor particles. There are four steps in this search algorithm:

First, divide the computational domain into uniform grids and specify an index number for each grid. This index number is related to the spatial position of the grid. A simple index number can be the size of the grid's coordinates multiplied by space.

For example, if we divide a space which the size is 256^3 , and the grid as position is $(0x2, 0x3, 0x4)$, we set the index number to be calculated this way $(0x2, 0x3, 0x4) \cdot (0x100, 0x100, 0x100) = 0x020304$. So the index number of this grid with position $(0x2, 0x3, 0x4)$ should be $0x020304$.

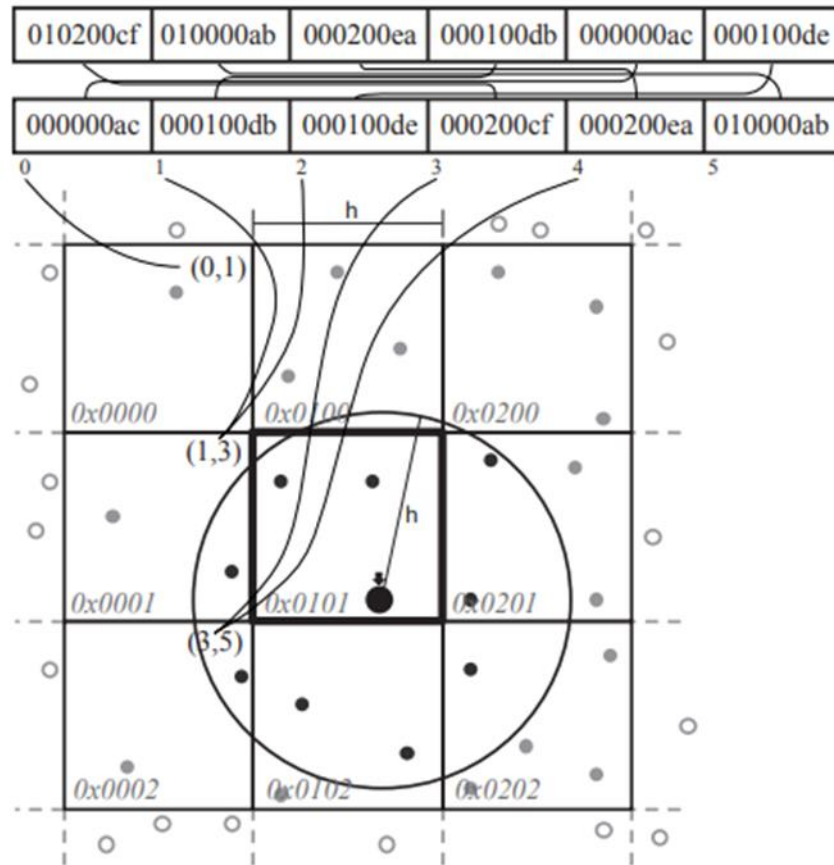


Figure 4-1: build grid index number [87].

Second, after every time step calculation, compute which grid and the index number of grid each particle belongs to based on the particle's position. Then, put the index number of the grid in high 32 bit and put the index number of particles in low 32 bit. So a new 64 bit number will be generated.

Third, reorder the new 64 bits long int numbers. Due to the index number of the grid being set at high 32 bits, the index number of particles will continue in GPU's memory. The order of the new 64 bits number is based on the index number of grids.

The last step, judge where the starting point is and end point for one grid. If the previous 64 bits index number has a different high 32 bits with the following 64 bits index number, it means it is the starting point for a new grid.

In this way, it is easy to calculate the nearest particles for a huge number of particles simulation.

4.3.3 Tree search algorithm

The tree search method is very suitable for solving problems with variable smooth lengths. This algorithm constructs a tree through the position of the particles. Once the tree structure is constructed, it can efficiently search for the nearest neighbors. Therefore, the tree search method is particularly suitable for solving problems with a variable smooth length and a large number of particles. The degree of complexity of the tree search method is $O(N \lg N)$.

4.4 Shifting algorithm

To counter the anisotropic particle spacing, proposed a particle shifting algorithm to prevent the instabilities. The algorithm was first created for incompressible SPH, but can be extended to the weakly compressible SPH model used in this simulation.

An improvement on the initial shifting algorithm was proposed by who used Fick's first law of diffusion to control the shifting magnitude and direction. Fick's first law connects the diffusion flux to the concentration gradient:

$$J = -D_F \nabla C \quad \text{Eq. 4-9}$$

Where J is the flux, C the particle concentration, and D_F the Fickian diffusion coefficient [68]. Assuming that the flux, i.e. the number of particles passing through a unit surface in unit time, is proportional to the velocity of the particles, a particle shifting

velocity and subsequently a particle shifting distance can be found. Using the particle concentration, the particle shifting distance δr_s is given by:

$$\delta r_s = -D \nabla C_i \quad \text{Eq. 4-10}$$

Where D is a new diffusion coefficient that controls the shifting magnitude and absorbs the constants of proportionality. The gradient of the particle concentration can be found through an SPH gradient operator:

$$\nabla C_i = \sum_j \frac{m_j}{\rho_j} \nabla W_{ij} \quad \text{Eq. 4-11}$$

The proportionality coefficient D is computed through a form proposed by. It is set to be large enough to provide effective particle shifting, while not introducing significant errors or instabilities. This is achieved by performing a Von Neumann stability analysis of the advection-diffusion equation:

$$D \leq \frac{1}{2} \frac{h^2}{\Delta t_{\max}} \quad \text{Eq. 4-12}$$

Where Δt_{\max} is the maximum local time step that is permitted by the CFL condition for a given local velocity and particle spacing. The CFL condition states that:

$$\Delta t_{\max} \leq \frac{h}{\|u\|_i} \quad \text{Eq. 4-13}$$

From equation above we can derive an equation to find the shifting coefficient D :

$$D = Ah \|u\|_i dt \quad \text{Eq. 4-14}$$

Where A is a dimensionless constant that is independent of the problem setup and discretization and dt is the current time step. Values in the range from 1 to 6 are proposed with 2 used as default.

To counter this effect, proposed a free-surface correction that limits diffusion to the surface normal but allow shifting on the tangent to the free surface. Therefore, this correction is only used near the free surface, identified by the value of the particle divergence, which is computed through the following equation, first proposed by:

$$\nabla \cdot \mathbf{r} = \sum_j \frac{m_j}{\rho_j} \mathbf{r}_{ij} \cdot \nabla_i W_{ij} \quad \text{Eq. 4-15}$$

This idea is applied to the code by multiplying the shifting distance of Eq. 2-78 with a free-surface correction coefficient A_{FSC} :

$$A_{FSC} = \frac{\nabla \cdot \mathbf{r} - A_{FST}}{A_{FSM} - A_{FST}} \quad \text{Eq. 4-16}$$

where A_{FST} is the free-surface threshold and A_{FSM} is the maximum value of the particle divergence. The latter depends on the domain dimensions:

$$A_{FSM} = \begin{cases} 2 & 2D \\ 3 & 3D \end{cases} \quad \text{Eq. 4-17}$$

$$A_{FST} = \begin{cases} 1.5 & 2D \\ 2.75 & 3D \end{cases}$$

4.5 Boundary condition

In the SPH method, an algorithm has a defect when the particles are close to the boundary. So the SPH method may not be suitable for all computational domains. This will affect the stability of the numerical simulation results and the accuracy of the calculation, so the boundary conditions need to be adjusted [44]. For the solid boundary condition, there is no universally accepted method. The existing methods generally lack strict precision analysis. It is difficult to balance the accuracy of calculations, the complexity of the computational area during the calculation.

4.5.1 The repulsive boundary conditions

The repulsive boundary condition is the distribution of fixed virtual particles in the boundary area. When the fluid particles close to the boundary, the virtual particles exert a repulsive force in the opposite direction on the fluid particles in order to prevent non-physical penetration of fluid particles to the boundary. The repulsive force between two particles i and j can be expressed as:

$$f_{ij} = \begin{cases} D \left[\left(\frac{r_0}{r_{ij}} \right)^{n_1} - \left(\frac{r_0}{r_{ij}} \right)^{n_2} \right] \frac{r_{ij}}{r_{ij}^2}, & r_{ij} < r_0 \\ 0, & r_{ij} > r_0 \end{cases} \quad \text{Eq. 4-18}$$

D is a parameter that depends on the specific problem. Its dimension is roughly equivalent to the square of the speed. This method is simple and easy. The disadvantage is that the value of each parameter in the function **Eq. 4-18** is not easy to determine and cannot accurately simulate the movement of particles near the boundary. If the parameter is not selected properly, the repulsion force will be too large or too small.

Another type of repulsive force is proposed by Monaghan:

$$B(x, y) = \Gamma(y)\chi(x) \quad \text{Eq. 4-19}$$

The expression of $\Gamma(y)$ and $\chi(x)$ are:

$$\Gamma(y) = \begin{cases} \frac{2}{3}, & 0 < q < h \\ 2q - \frac{3}{2}q^2, & \frac{2}{3} < q < 1 \\ \frac{1}{2}(2-q)^2, & 1 < q < 2 \\ 0 & \text{other} \end{cases} \quad \text{Eq. 4-20}$$

$$\chi(x) = \begin{cases} 1 - \frac{x}{\Delta x}, & 0 < x < \Delta x \\ 0, & \text{other} \end{cases} \quad \text{Eq. 4-21}$$

The function $\chi(x)$ is to ensure that the particles receive a constant force from the boundary when they move parallel to the boundary. Gomez-Gesteira *et al.* proposed to use boundary particles to balance the internal pressure and prevent the particles from crossing the boundary. The external layers of virtual particles have the same initial density as the particle in the calculation domain, and its speed is zero. The innermost virtual particles represent the solid boundary. In the initial state, they have the same density as the internal particles. Virtual particles on boundary layer calculate with internal particles together. The density of boundary particles is changing, but their speed is zero, which ensures that the boundary particles do not move. The advantage of this method is that the pressure on the boundary can be directly obtained by the simulation, and the precision is good. The disadvantage is that the velocity of particles which is close to the solid boundary is greatly affected by the boundary. The virtual particles are fixed and will produce larger numerical dissipation [51].

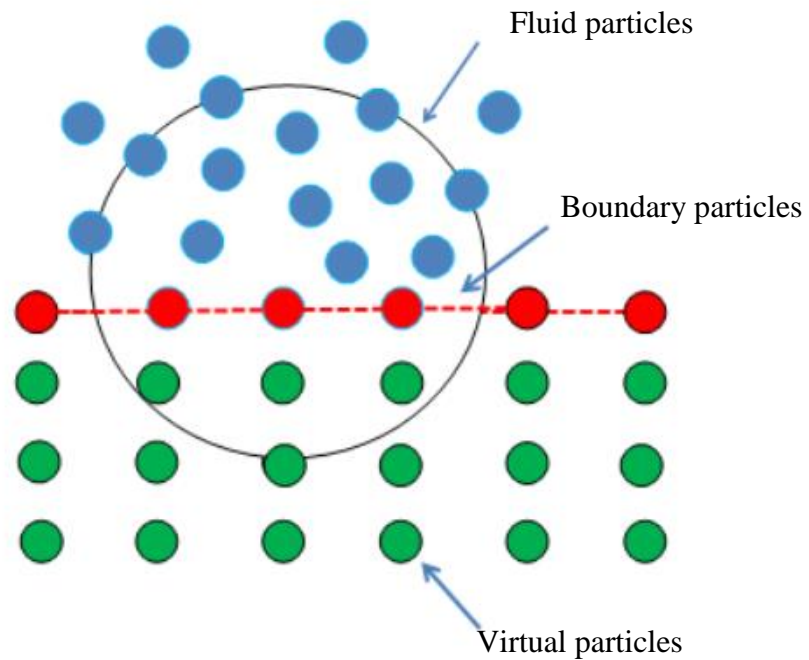


Figure 4-2: the repulsive boundary condition [27].

4.5.2 Dynamic Boundary Condition

This method sees boundary particles that satisfy the same equations as fluid particles. However, they do not move according to the forces exerted on them. Instead, they remain either fixed in position or move according to an imposed motion function.

When a fluid particle approaches a boundary and the distance between its particles and the fluid particle becomes smaller than twice the smoothing length (h), the density of the affected boundary particles increases, resulting in a pressure increase. In turn, this results in a repulsive force being exerted on the fluid particle due to the pressure term in the momentum equation. Stability of this method relies on the length of time step taken being suitably short in order to handle the highest present velocity of any fluid

particles currently interacting with boundary particles and is therefore an important point when considering how the variable time step is calculated.

4.5.3 Periodic boundary

The main idea of periodic boundary conditions is that the number of particles is constant in the entire numerical simulation process. If there are particles moving out of the interface, the same particles must be returned to the model from the opposite interface. If the particles move outside of the boundary, the corresponding particles enter the boundary from the other side, thus ensuring that the number of particles in the system is constant.

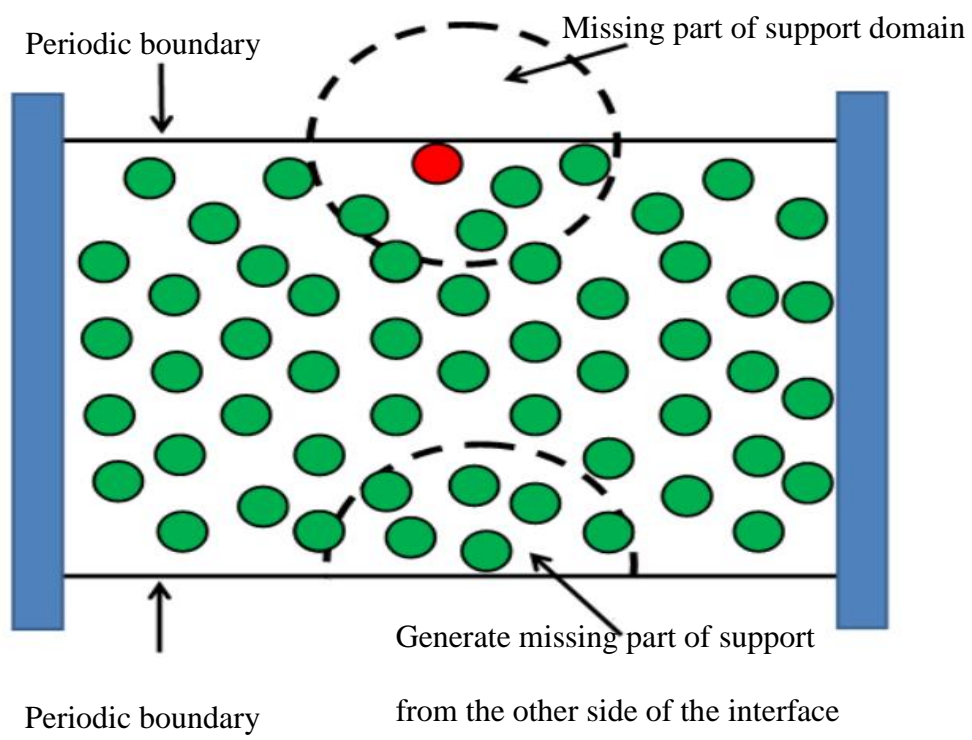


Figure 4-3: the periodic boundary condition [27].

4.6 Result and discussion

4.6.1 Parameters and details about simulation

In this section, the 3-D thrombus simulation is established. There are three components in this model: erythrocyte as floating objects, blood flow as fluid particles, and vessel model as the boundary. The total number of particles in thrombus simulation is about 1 million. The erythrocyte is a round cake shaped object with a bulging edge. In thrombus simulation, the shape of erythrocyte model is the same as in reality. One erythrocyte consists of 1382 particles. The diameter and thickness are $8 \mu\text{m}$ and $2.5 \mu\text{m}$.

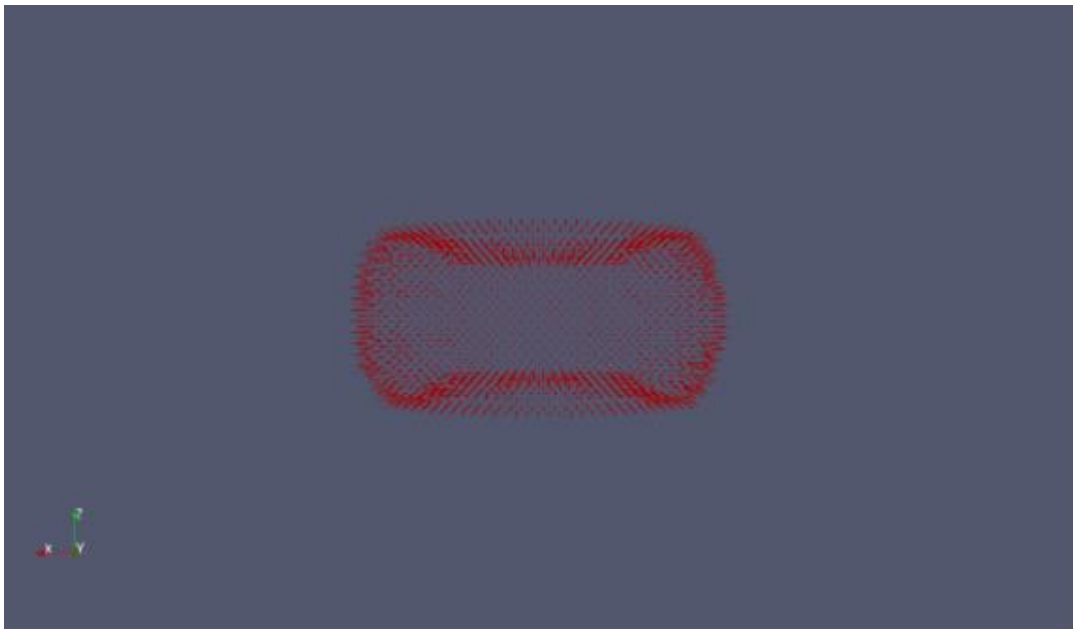


Figure 4-4: the vertical perspective of erythrocyte.

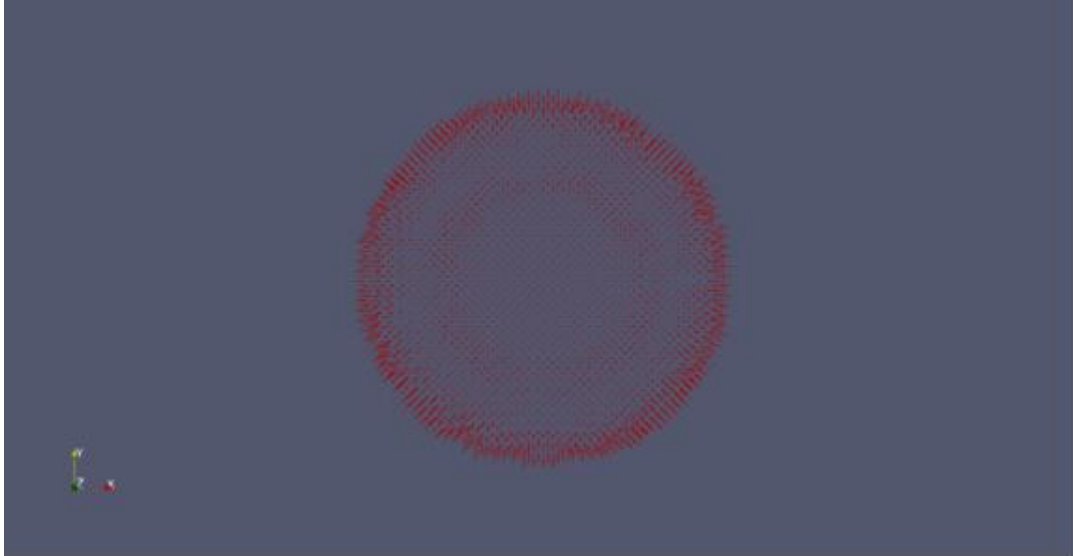


Figure 4-5: The horizontal perspective of erythrocyte.

The length and diameter of the vessel model are 2 *mm* and 0.04 *mm*. In order to achieve satisfied results, a control group was added. There are two models, one is 25% stenosis of a cross-section blood vessel model and the other is 75% stenosis of a cross-section blood vessel model.



Figure 4-6: initial condition of the 25% cross-section stenosis blood vessel model.



Figure 4-7: initial condition of the 75% cross-section stenosis blood vessel model.

The narrow part of the blood vessel represents the presence of a thrombus.

Comparing the results of the two simulation models illustrate the impact of thrombosis on the blood flow.

4.6.2 Velocity of blood flow in two models

Abstract floating objects from simulation, erythrocytes have obvious congestion before entering the stenotic channel of blood vessels in a 75% cross-section stenosis blood vessel model, as shown in **Figure 4-8**. However, the distribution of red blood cells is relatively uniform in 25% cross-section stenosis blood vessel model in **Figure 4-9**. This indicates that the thrombus has hindered the passage of the blood flow. There are simulation results that can also indicate the velocity of the blood flow in the 25% cross-section stenosis blood vessel model is faster than the other. Slower blood flow is more conducive to the formation and growth of blood clots. Erythrocytes are the most abundant type of blood cells in the blood.



Figure 4-8: erythrocytes in 25% cross-section stenosis blood vessel model.

They are also the most important mediators of oxygen transport in vertebrates, and they also have immune functions. When it is hard for erythrocytes to enter the tissue through the capillaries, it will cause local hypoxia.



Figure 4-9: erythrocytes in 75% cross-section stenosis blood vessel model.

4.6.3 Compare results with other simulation and experimental data

The presence of a thrombus results in a narrow cross-section of the blood vessel , and after the blood has flowed through the blocked part, a blood jet is formed and will create a small vortex near the wall of the blood vessel. The Oxford University's researchers got similar result by DNS, as shown in **Figure 4-11**.

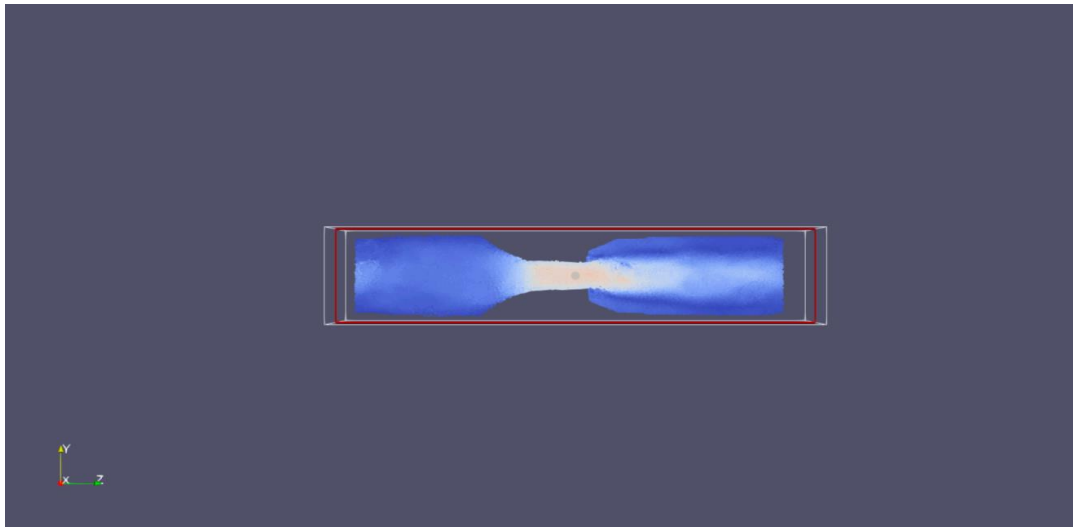


Figure 4-10: cross-section of 75% stenosis blood vessel model.

Actually, the starting vortex formed during early acceleration, at the jet front as the fluid accelerated through the stenosis, started to break up into elongated stream wise structures, though the flow remained laminar at this point. This phenomenon will only happen when high viscosity fluid passes a narrow channel.

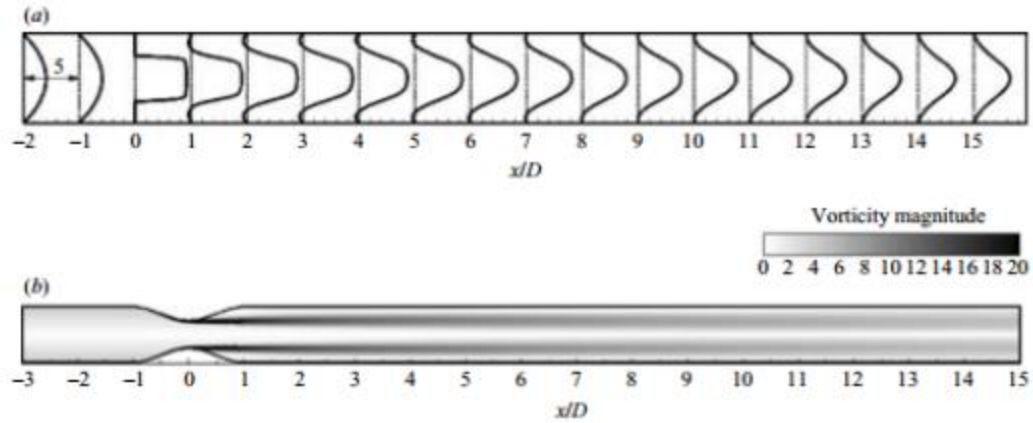


Figure 4-11: pulsatile flow through the 75 % axisymmetric stenosis [88].

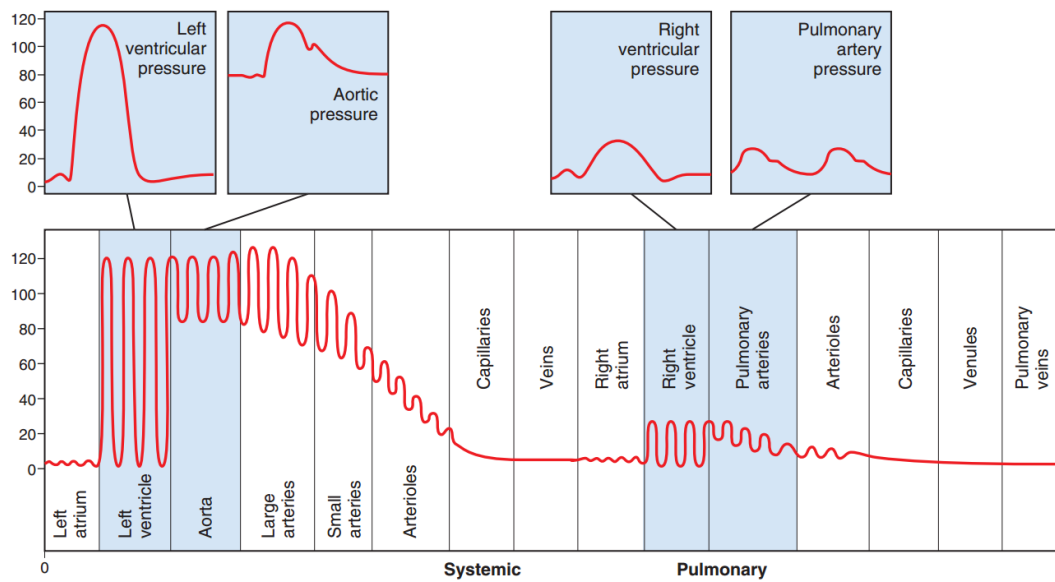


Figure 4-12: human normal blood pressure range [89].

The range of blood pressure in arterial blood from 20 mmHg to 60 mmHg from medical reference **Figure 4-12**. Convert the unit to Pascal, and the blood pressure is about 5333 Pa to 2666 Pa. This is the average value for the pressure of the arterial.

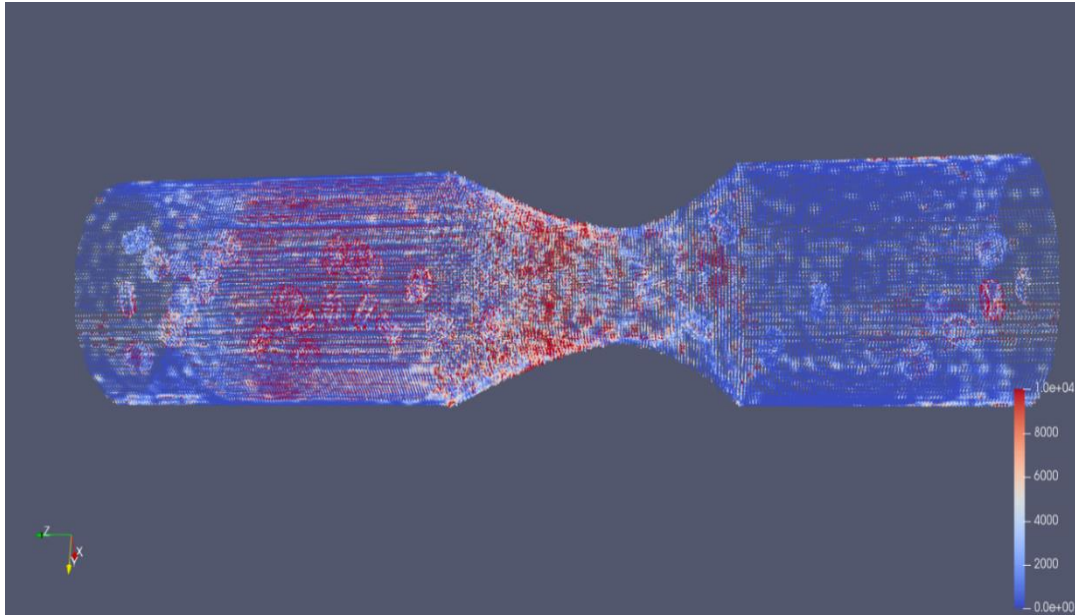


Figure 4-13: pressure of 75% cross-section stenosis blood vessel model.

In my simulation, this means that the peak blood pressure for capillaries is about 5666 Pa. In the 75% cross-section stenosis blood vessel model, the peak blood pressure of boundary stenosis part is around 9000~10000 Pa. Due to the presence of thrombus, the pressure at the thrombus site is much higher than the normal value. The simulation results match the experimental measurement.

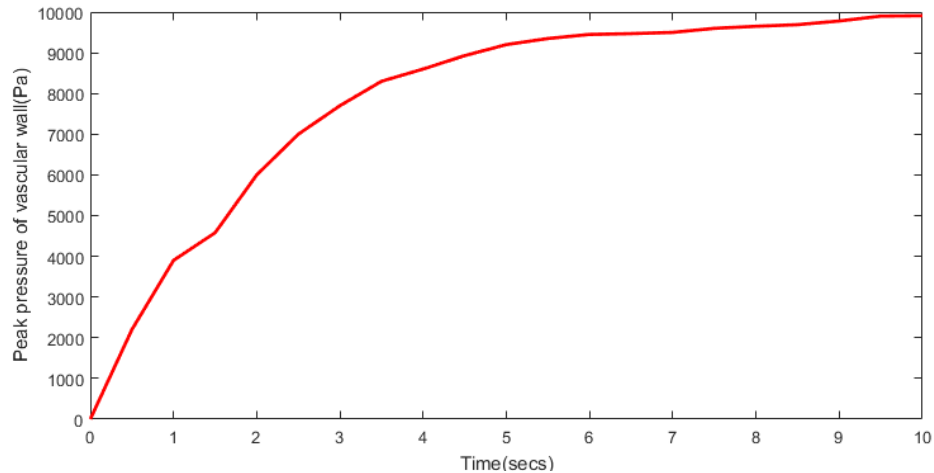


Figure 4-14: peak pressure of the 75% cross-section stenosis blood vessel model.

In the above figure, the plot indicates the peak pressure of blood vessel wall during the entire simulation process. At the beginning, the blood flow is motionless, so the pressure equal to 0, then a force is added on the inlet's surface. After several secs, the system becomes more stable. The peak pressure of the 75% cross-section stenosis blood vessel is around 10000 Pa. The peak pressure of the 25% cross-section stenosis blood vessel is only around 5500 Pa.

4.7 Conclusion

It could be illustrated from the thrombus simulation results that with the blocked area increasing, the velocity of the blood flow slows down significantly before passing through the thrombus. Erythrocytes will be more easily deposited at the site of the thrombus, and further increasing the size of the thrombus. With age increasing, the elasticity of the blood vessel wall gradually weakens. On the one hand, the presence of thrombus will greatly hinder red blood cells from delivering oxygen causing hypoxia, and

on the other hand, with the increasing of thrombosis, it is very easy to cause the rupture of blood vessels.

Due to the presence of thrombus, the pressure and shear force on the boundary near the thrombus will rise, which will promote the formation of new thrombus and promote its growth. This simulation study has analyzed the velocity of the blood flow and vascular wall pressure with the different size of the thrombus. The simulation results are compared with the experimental data and simulation data, confirming the correctness of the simulation results. Because the model is closer to the real situation of the human body than the previous blood vessel simulation model, the result of this simulation is more persuasive. The simulation provided the basis for further understanding and prevention of thrombosis formation conditions, formation site, and thrombosis.

CHAPTER 5

CONCLUSIONS

5.1 Summary

In this dissertation, I use the SPH method to solve flows with different boundary conditions and scales in medical and biological engineering. In Chapter 2, literature reviews for the basic theory includes kernel function approximation and particle approximation. This chapter also introduces advanced techniques of the SPH method, such as viscosity term selection, boundary condition selection, and time steps selection. In Chapter 3, two-dimensional and three-dimensional simulations of the microneedle diffusion are presented. SPH result indicates the average concentration in deeper layer is about 0.0054 mol/m^3 , and SEM shows the minimum contraction at interface layer is about $5.296 \times 10^{-3} \text{ mol/m}^3$. These results demonstrate that the dosage in the deeper layers in SEM and SPH models are beyond 0.004267 mol/m^3 , the minimum concentration. Results from the mesh-based SEM and the mesh-free SPH simulations revealed details about the processes of delivery of medicine particles through microneedles and diffusion in the skin tissue, and the medicine concentration change with space and time. The overall effect of medicine delivery under initial concentration and conditions were simulated and the effect of drug delivery were assessed.

Chapter 4 is the modeling of blood vessel simulation with thrombus. By comparing the results of two simulations with 25% and 75% stenosis conditions in blood

vessel illustrate the impact of thrombosis on blood flow and blood vessel wall. Because the model close to the real situation of the human body than the previous blood vessel simulation model, the result of this simulation is more persuasive. The pressure of blood flow in 0.04 *mm* diameter blood vessel is around 5000 Pa, which matches the medical reference. The increase of blood pressure in blood vessel with 75% stenosis could be measured in this simulation. The peak pressure of blood in blood vessel with 75% stenosis is around 10000 Pa. The internal environment of a human is hard to observe and measure. Blood pressure is a very essential factor to cause cardiovascular and cerebrovascular diseases. This simulation provides an important reference for research of arterioles thrombus and the impact of arterioles thrombus on blood flow and pressure increasing.

5.2 Future work

Due to its Lagrangian character, the local resolution of SPH follows the particles flow, and it is convenient in representing the large density changes problems often encountered in fluid problems, engineering problems and some biological problems. Based on these characteristics [91], I will develop the microneedle and arterioles thrombus models, and try to use more particles to operate simulation. If using several million particles, it will bring some new challenges. First, the code needs to convert to the operating platforms from Windows to Linux. Most of the HPC centers use Linux as their operating system. The second, more GPUs should be added as calculation units. Mpi and openmp will also be included in these projects for accelerate the calculation [92]. Another development direction is that based on existing arterioles thrombus model, part of vessel stenosis could use viscous particles to replace stenosis pattern. In this way, this

simulation could also study the processing of thrombus formation and thrombus deformation.

BIBLIOGRAPHY

- [1] Lucy L. B. A numerical approach to the testing of the fission hypothesis. *Astronomical Journal*, 1977, 82(12):1013-1024.
- [2] Gingold R. A. ,Monaghan J. J. Smoothed particle hydrodynamics-Theory and application to non-spherical stars. *Monthly notices of the royal astronomical society*,1977,181:375-389.
- [3] Monaghan J. J. Smoothed particle hydrodynamics. *Reports on Progress in Physics*, 2005,68(8): 1703-1759.
- [4] Liu M. B. ,Liu G. R. Smoothed Particle Hydrodynamics (SPH): an Overview and Recent Developments. *Archives of Computational Methods in Engineering*, 2010,17(1):25-76.
- [5] Monaghan J. J. Smooth particle hydrodynamics. *Annual review of astronomy and astrophysics*, 1992,30:543-574.
- [6] Monaghan J. J. ,Lattanzio J. C. A simulation of the collapse and fragmentation of cooling molecular clouds. *Astrophysical Journal*, 1991,375(1):177-189.
- [7] Lee W. H. Newtonian hydrodynamics of the coalescence of black holes with neutron stars- III. Irrotational binaries with a stiff equation of state. *Monthly Notices of the Royal Astronomical Society*, 2000,318(2):606-624.
- [8] Monaghan J. J. Modelling the universe. *Astronomical Society of Australia Proceedings*, 1990,8(3):233-237.
- [9] Monaghan J. J. ,Kos A. Solitary waves on a Cretan beach. *Journal Of Waterway Port Coastal And Ocean Engineering-ASCE*, 1999,125(3):145-154.
- [10] Monaghan J. J. ,Kocharyan A. SPH simulation of multi-phase flow. *Computer Physics Communications*, 1995,87(1-2):225-235.
- [11] Colagrossi A. ,Landrini M. Numerical simulation of interfacial flows by smoothed particle hydrodynamics. *Journal of Computational Physics*, 2003,191(2):448-475.

- [12] Shao S. D. SPH simulation of solitary wave interaction with a curtain-type breakwater. *Journal of Hydraulic Research*, 2005,43(4):366-375.
- [13] Gomez-Gesteira M. ,Dalrymple R. A. Using a three-dimensional smoothed particle hydrodynamics method for wave impact on a tall structure. *Journal of Waterway Port Coastal and Ocean Engineering-Asce*, 2004,130(2):63-69.
- [14] Dalrymple R. A. ,Rogers B. D. Numerical modeling of water waves with the SPH method. *Coastal Engineering*, 2006,53(23):141-147.
- [15] Gotoh H., Shao S. D., Memita T. SPH-LES model for numerical investigation of wave interaction with partially immersed breakwater. *Coastal Engineering*, 2004,46(1):39-63.
- [16] Yim S. C., Yuk D., Panizzo A., Di Risio M., Liu P. L. F. Numerical Simulations of wave generation by a vertical plunger using RANS and SPH models. *Journal of Waterway Port Coastal and Ocean Engineering-Asce*, 2008,134(3):143-159.
- [17] Cleary P. W. ,Prakash M. Discrete-element modelling and smoothed particle hydrodynamics: potential in the environmental sciences. *Philosophical Transactions: Mathematical, Physical and Engineering Sciences*, 2004,362(1822):2003-2030.
- [18] Liang D.-f., Thusyanthan N. I., Madabhushi S. P. G., Tang H.-w. Modelling solitary waves and its impact on coastal houses with SPH method. *China Ocean Engineering*, 2010,24(2):353-368.
- [19] Zheng K., Sun Z.-c., Sun J.-w. Numerical simulation of water wave dynamics based on SPH method. *Journal of Hydrodynamics*, 2009,21(6):843-850.
- [20] Libersky L. D., Randles P. W., Carney T. C., Dickinson D. L. Recent improvements in SPH modeling of hypervelocity impact. *International Journal of Impact Engineering*, 1997,20(6):525-532.
- [21] Attane P., Girard F., Morin V. An energy balance approach of the dynamics of drop impact on a solid surface. *Physics of Fluids*, 2007,19(1):012101-012112.
- [22] Gomez-Gesteira, Moncho, et al. "SPHysics – development of a free-surface fluid solver – Part 1: Theory and formulations." *Computers & Geosciences* 48 (2012): 289-299.
- [23] Gómez-Gesteira, Moncho, et al. "SPHysics – development of a free-surface fluid solver – Part 2: Efficiency and test cases." *Computers & Geosciences* 48 (2012): 300-307.

- [24] Crespo, Alejandro JC, et al. "DualSPHysics: Open-source parallel CFD solver based on Smoothed Particle Hydrodynamics (SPH)." *Computer Physics Communications* 187 (2015): 204-216.
- [25] Loren-Aguilar, Pablo, and Matthew R. Bate. "Two-fluid dust and gas mixtures in smoothed particle hydrodynamics II: an improved semi-implicit approach (Dataset)." (2015).
- [26] Mao, Wenbin, et al. "Fully-coupled Fsi Simulation of Bioprosthetic Heart Valve Using Smoothed Particle Hydrodynamics." *Cardiology* 134.2 (2016): 178.
- [27] Lind, S. J., P. K. Stansby, and Benedict D. Rogers. "Incompressible - compressible flows with a transient discontinuous interface using smoothed particle hydrodynamics (SPH)." *Journal of Computational Physics* 309 (2016): 129-147.
- [28] Lind, S. J., P. K. Stansby, and Benedict D. Rogers. "Incompressible - compressible flows with a transient discontinuous interface using smoothed particle hydrodynamics (SPH)." *Journal of Computational Physics* 309 (2016): 129-147.
- [29] Fourtakas, G., and B. D. Rogers. "Modelling multi-phase liquid-sediment scour and resuspension induced by rapid flows using Smoothed Particle Hydrodynamics (SPH) accelerated with a Graphics Processing Unit (GPU)." *Advances in water resources* 92 (2016): 186-199.
- [30] Albano, Raffaele, et al. "Modelling large floating bodies in urban area flash-floods via a Smoothed Particle Hydrodynamics model." *Journal of Hydrology* 541 (2016): 344-358.
- [31] Caballero, Andrés, et al. "Modeling left ventricular blood flow using smoothed particle hydrodynamics." *Cardiovascular engineering and technology* 8.4 (2017): 465-479.
- [32] Swegle J. W. ,Attaway S. W. On the feasibility of using Smoothed Particle Hydrodynamics for underwater explosion calculations. *Computational Mechanics*,1995,17(3):151-168.
- [33] Nasiri, Hossein, et al. "A smoothed particle hydrodynamics approach for numerical simulation of nano-fluid flows." *Journal of Thermal Analysis and Calorimetry* (2018): 1-9.
- [34] Alia A. ,Souli M. High explosive simulation using multi-material formulations. *Applied Thermal Engineering*, 2006,26(10):1032-1042.
- [35] Liu M. B., Liu G. R., Lam K. Y., Zong Z. Meshfree particle simulation of the

detonation process for high explosives in shaped charge unlined cavity configurations. *Shock Waves*, 2003,12(6):509-520.

- [36] Liu M. B., Liu G. R., Zong Z., Lam K. Y. Computer simulation of high explosive explosion using smoothed particle hydrodynamics methodology. *Computers & Fluids*, 2003,32(3):305-322.
- [37] Liu M. B., Liu G. R., Lam K. Y. Investigations into water mitigation using a meshless particle method. *Shock Waves*, 2002,12(3):181-195.
- [38] Liu M. B., Liu G. R., Lam K. Y., Zong Z. Smoothed particle hydrodynamics for numerical simulation of underwater explosion. *Computational Mechanics*, 2003,30(2):106-118.
- [39] Morris J. P., "Analysis of smoothed particle hydrodynamics with applications," PhD Thesis, Monash University, 1996.
- [40] Kikuchi M., Miyamoto B. Numerical simulation of impact crush/buckling of circular tube using SPH method. *Key Engineering Materials*, 2006,306-308:697-702.
- [41] Du, Qiang, Richard B. Lehoucq, and Alexandre M. Tartakovsky. "Integral approximations to classical diffusion and smoothed particle hydrodynamics." *Computer Methods in Applied Mechanics and Engineering* 286 (2015): 216-229.
- [42] Limido J., Espinosa C., Salaun M., Lacombe J. L. SPH method applied to high speed cutting modelling. *International Journal of Mechanical Sciences*, 2007,49(7):898-908.
- [43] Liu, Mou-bin, Can Huang, and A-man Zhang. "Modelling incompressible flows and fluid-structure interaction problems with smoothed particle hydrodynamics: Briefing on the 2017 SPHERIC Beijing International Workshop." *Journal of Hydrodynamics* 30.1 (2018): 34-37.
- [44] Hui H. H., Fukagawa R., Sako K. Smoothed particle hydrodynamics for soil mechanics. *Terramechanics*, 2006,26:49-53.
- [45] Ha J., Cleary P. W. Comparison of SPH simulations of high pressure die casting with the experiments and VOF simulations of Schmid and Klein. *International Journal of Cast Metals Research*, 2000,12(6):409-418.
- [46] Tartakovsky, Alexandre M., et al. "Smoothed particle hydrodynamics and its applications for multiphase flow and reactive transport in porous media." *Computational Geosciences* 20.4 (2016): 807-834.
- [47] Wang W., Huang Y., Grujicic M., Chrisey D. B. Study of impact-induced mechanical effects in cell direct writing using smooth particle hydrodynamic

method. *Journal of Manufacturing Science and Engineering-Transactions of the Asme*, 2008,130(2):12-21.

- [48] Liu M. B., Chang J. Z., Li H. Q., "Numerical modeling of injection flow of drug agents for controlled drug delivery," in 2007 Annual International Conference of the Ieee Engineering in Medicine and Biology Society, Vols 1-16, 2007, pp. 1152-1155.
- [49] Crespo A. J. C., Gomez-Gesteira M., Dalrymple R. A. Modeling dam break behavior over a wet bed by a SPH technique. *Journal of Waterway Port Coastal and Ocean Engineering-Asce*, 2008,134(6):313-320.
- [50] Vaikuntanathan V., Kannan R., Sivakumar D. Impact of water drops onto the junction of a hydrophobic texture and a hydrophilic smooth surface. *Colloids and Surfaces a-Physicochemical and Engineering Aspects*, 2010,369(1-3):65-74.
- [51] Altomare, Corrado, et al. "Applicability of smoothed particle hydrodynamics for estimation of sea wave impact on coastal structures." *Coastal Engineering* 96 (2015): 1-12.
- [52] Belytschko T., Krongauz Y., Organ D., Fleming M., Krysl P. Meshless methods: An overview and recent developments. *Computer Methods in Applied Mechanics and Engineering*, 1996,139(14):3-47.
- [53] Shadloo, M. S., G. Oger, and David Le Touzé. "Smoothed particle hydrodynamics method for fluid flows, towards industrial applications: Motivations, current state, and challenges." *Computers & Fluids* 136 (2016): 11-34.
- [54] Swegle J. W., Hicks D. L., Attaway S. W. Smoothed particle hydrodynamics stability analysis. *Journal of Computational Physics*, 1995,116(1):123-134.
- [55] Liu M. B., Liu G. R., Lam K. Y. Constructing smoothing functions in smoothed particle hydrodynamics with applications. *Journal of Computational and Applied Mathematics*, 2003,155(2):263-284.
- [56] Xiao S. P. ,Belytschko T. Material stability analysis of particle methods. *Advances in Computational Mathematics*, 2005,23(1):171-190.
- [57] Hicks D. L. ,Liebrock L. M. Conservative smoothing with B-splines stabilizes SPH material dynamics in both tension and compression. *Applied Mathematics and Computation*, 2004,150(1):213-234.
- [58] Wang L., Ge W., Li J. A new wall boundary condition in particle methods. *Computer Physics Communications*, 2006,174(5):386-390.
- [59] Liu M. B. ,Chang J. Z. A new boundary treatment algorithm for dissipative particle dynamics. *Acta Physica Sinica*, 2010,59(11):26-33.

- [60] Liu M. B., Shao J.R ,Chang J. Z. On the treatment of solid boundary in smoothed particle hydrodynamics. .Science China Technological Sciences,2012,55(1):244-254.
- [61]Shadloo, M. S., G. Oger, and David Le Touzé. "Smoothed particle hydrodynamics method for fluid flows, towards industrial applications: Motivations, current state, and challenges." *Computers & Fluids* 136 (2016): 11-34.
- [62] Li S. ,Liu W. K., *Meshfree Particle Methods*: Springer, 2004.
- [63] Liu M. B. ,Liu G. R. Smoothed particle hydrodynamics: some recent developments in theory and applications. *J. Beijing Polytech. Univ.*, 2004,30(61-71).
- [64] Liu G. R. ,Liu M. B., *Smoothed particle hydrodynamics: a meshfree particle method*. Singapore: World Scientific, 2003.
- [65] Ghazanfarian, J., R. Saghatchi, and D. V. Patil. "Implementation of Smoothed-Particle Hydrodynamics for non-linear Pennes' bioheat transfer equation." *Applied Mathematics and Computation* 259 (2015): 21-31.
- [66] Monaghan J. J. Particle methods for hydrodynamics. *Computer Physics Reports*, 1985,3:71-124.
- [67] Morris J. P. A study of the stability properties of smooth particle hydrodynamics. *PUBLICATIONS OF THE ASTRONOMICAL SOCIETY OF AUSTRALIA*, 1996,13(1):97-102.
- [68]Monaghan J. J. SPH without a tensile instability. *Journal Of Computational Physics*,2000,159(2): 290-311.
- [69] Liu M. B. ,Liu G. R. Restoring particle consistency in smoothed particle hydrodynamics. *Applied Numerical Mathematics*, 2006,56(1):19-36.
- [70] Li S. ,Liu W. K. Meshfree and particle methods and their applications. *Applied Mechanics Reviews*, 2002,55(1):1-34.
- [71] Chen J. K., Beraun J. E., Carney T. C. A corrective smoothed particle method for boundary value problems in heat conduction. *International Journal for Numerical methods in Engineering*, 1999,46(2):231-252.
- [72] Chen J. K., Beraun J. E., Jih C. J. An improvement for tensile instability in smoothed particle hydrodynamics. *Computational Mechanics*, 1999,23(4):279-287.
- [73] Liu W. K., Chen Y., Jun S., Chen J. S., Belytschko T., Pan C., Uras R. A., Chang C. T. Overview and applications of the reproducing kernel particle methods. *Archives of Computational Methods in Engineering*, 1996,3(1):3-80.

- [74] Atluri S. N., Han Z. D., Rajendran A. M. A new implementation of the meshless finite volume method, through the MLPG mixed approach. CMES: Computer Modeling in Engineering & Sciences, 2004,6(6):491-514.
- [75] Liu M. B., Xie W. P., Liu G. R. Modeling incompressible flows using a finite particle method. Applied Mathematical Modelling, 2005,29(12):1252-1270.
- [76] Monaghan J. J. On the problem of penetration in particle methods. Journal of Computational Physics, 1989,82(1):1-15.
- [77] Monaghan J. J. Why particle methods work. SIAM JOURNAL ON SCIENTIFIC AND STATISTICAL COMPUTING, 1982,3(4):422-433.
- [78] Liu M. B., Shao J. R., Chang J. Z. On the treatment of solid boundary in smoothed particle hydrodynamics. Science China Technological Sciences, 2012,55(1):244-254.
- [79] Morris J. P., Fox P. J., Zhu Y. Modeling low Reynolds number incompressible flows using SPH. Journal of Computational Physics, 1997,136(1):214-226.
- [80] Monaghan J. J. Simulating free surface flows with SPH. Journal of Computational Physics, 1994,110(2):399-406.
- [81] Monaghan J. J. Simulating free surface flows with SPH. Journal of Computational Physics, 1994,110(2):399-406.
- [82] Morris J. P., "Analysis of smoothed particle hydrodynamics with applications," PhD, Department of Mathematics, Monash University, Melbourne, Australia, 1996.
- [83] Monaghan J. J., Kos A. Solitary waves on a Cretan beach. Journal of Waterway, Port, Coastal, and Ocean Engineering, 1999,125(6):250-259
- [84] Liu M. B., Liu G. R. Meshfree particle simulation of micro channel flows with surface tension. Computational Mechanics, 2005,35(5):332-341.
- [85] Zhang, Haibo. Computational micro-flow with spectral element method and high Reynolds number flow with discontinuous Galerkin Finite Element Method. Diss. Louisiana Tech University, 2016.
- [86] Liu, Don, et al. "Mesh-free GPU Simulation of Complex Flows in Three Dimensional Distorting Domain." International Journal of Scientific and Innovative Mathematical Research 3.1 (2015): 6-17.
- [87] Auer S. Realtime particle-based fluid simulation.
- [88] Varghese, Sonu S., Steven H. Frankel, and Paul F. Fischer. "Direct numerical simulation of stenotic flows. Part 2. Pulsatile flow." Journal of Fluid Mechanics 582 (2007): 281-318.

- [89] Guyton, Arthur C., et al. "Brief reviews: a systems analysis approach to understanding long-range arterial blood pressure control and hypertension." *Circulation Research* 35.2 (1974): 159-176.
- [90] Carlos, "Smoothed particle hydrodynamics" Instituto de Física - UFRJ
- [91] Wang, Yifan. *Numerical solutions for problems with complex physics in complex geometry*. Louisiana Tech University, 2014.
- [92] Wang, Yifan, Annalisa Quaini, and Sunčica Čanić. "A Higher-Order Discontinuous Galerkin/Arbitrary Lagrangian Eulerian Partitioned Approach to Solving Fluid–Structure Interaction Problems with Incompressible, Viscous Fluids and Elastic Structures." *Journal of Scientific Computing* (2018): 1-40.